DEVELOPMENT OF AN AREAL SNOW DEPLETION CURVE IN THE DRY CREEK EXPERIMENTAL WATERSHED USING MODIS SATELLITE IMAGERY AND THE UTAH ENERGY BALANCE SNOW ACCUMULATION AND MELT MODEL

by

Michael Procsal

A thesis

submitted in partial fulfillment

of the requirements for the degree of

Master of Science in Geology

Boise State University

December 2005

The thesis presented by Michael Procsal entitled Development of an Areal Snow Depletion Curve in the Dry Creek Experimental Watershed using MODIS Satellite Imagery and the Utah Energy Balance Snow Accumulation and Melt Model is hereby approved:

James McNamara Date
Advisor

Charles Luce Date
Committee Member

David Wilkins Date
Committee Member

John R. Pelton Date
Dean, Graduate College

ACKNOWLEDGEMENTS

Without the help of many individuals this thesis would not have been possible. I would like to extend my thanks to my advisor Jim McNamara for his availability both in the office and in the field. His assistance was instrumental in solving the day-to-day problems I encountered throughout the duration of this research. Many thanks to Charlie Luce for technical assistance with the UEB snowmelt model. His ability to explain complicated things in a simple way was very supportive and motivational. Thanks to Dave Wilkins who introduced me to the world of remote sensing and the capabilities of satellite imagery.

Special thanks to Justin Huntington for data processing and the utilization of his resources at other unmentionable universities besides Boise State University.

Thanks to Greg Oldenborger and James Nelson for their programming knowledge. Without their code, it would have taken several more months to complete this research.

Funding was provided from NASA Epscor grant, Boise State University through a teaching assistanceship, and Geological Society of America.

To all those that helped with data collection in the field: Jim McNamara, Patrick Kormos, Eric Rothwell, Jason Williams, Justin Huntington, and Marc Buursink.

Lastly, thank you most gratefully to my family, Jennifer and Lauren for emotional support and inspiration.

ABSTRACT

An areal depletion curve that relates fractional snow covered area (SCA_{af}) to snow water equivalent (SWE) is developed using moderate resolution imaging spectroradiometer (MODIS) and the Utah Energy Balance Snow Accumulation and Melt model (UEB). The depletion curve presented here is defined as a graphical representation of the depletion of snow with SCA_{af} as the y-axis and SWE normalized to the maximum SWE (W_a/W_{amax}) as the x-axis. The results demonstrate that snowpack heterogeneity within the entire Dry Creek Experimental Watershed is well characterized by the derived depletion curve. Results also indicate that the snowpack has a bimodal distribution in parts of the basin and that snow variability cannot be captured with coefficients of variation alone. UEB results are compared to measured SWE values at Bogus Basins Snotel site and verify that melt dynamics are well simulated.

Depletion curves offer improvement to present day methods for predicting snowmelt and therefore snowmelt generated runoff in high mountain catchments. MODIS (Moderate Resolution Imaging Spectroradiometer) provides improved capabilities for observed snow cover with mean absolute error less than 0.1, and therefore aids in the development of these depletion curves. Using a normalized difference snow index (NDSI) approach to estimate fractional snow covered area (SCA_{af}) in 500 m pixels and modeling snow water equivalent (SWE) in 500 m pixels using the UEB snowmelt model, a functional form of a depletion curve is derived for the Dry Creek Experimental

Watershed, Boise, ID. The derived equation is transferable to any given year so that estimates of the water available for runoff can be made.

TABLE OF CONTENTS

1 INTRODUCTION

1.1 Scope

The hydrologic response from mountainous regions in North America is influenced primarily by the input of water that is stored as snow. Water stored as snow (snow water equivalent) doesn't enter the land phase of the hydrologic cycle until it melts. Therefore, it is of particular importance to understand how much water as snow is available for runoff and how it is distributed. Due to the high spatial and temporal variability in the physical processes that accumulate and melt snow it is difficult for hydrologists, water resource managers, and engineers to incorporate these effects into current operational streamflow forecasts. Methodology for predicting snow water equivalent (SWE) however, has improved significantly over the years especially with the more recent use of satellite imagery to get repeat measurements of snow covered area (SCA). Since the driving processes that melt snow only affect those areas covered by snow then the spatial pattern of SCA reduction is important. Understanding the inherent relationship between SCA and SWE offers potential advance in current methods used in hydrologic modeling.

1.2 Purpose

Development of hydrologic models for runoff forecasting in semi-arid high-mountain catchments rely heavily on the accurate estimation of spatially distributed snow water equivalence (SWE). As hydrologists and water resource managers, we are interested in the volume of water stored in snow that will serve as input into the land phase of the hydrologic cycle. Ideally, we would like to track this volume of water (SWE distributed spatially) over time, but this is a difficult task and present methods have inherent limitations. However, obtaining time series data of SCA using satellite imagery is a much easier and more accurate method for determining the spatial and temporal distribution of the snowpack.

A reduction in snow covered area (SCA) corresponds to a reduction in snow water equivalent (SWE) especially in rugged topography where snow cover is fractional. If a spatially and temporally consistent relationship exists between SCA and SWE then we can use one quantity to predict the other. Current snowmelt runoff models (Snowmelt Runoff Model (SRM) and National Weather Service River Forecast System-Snow Accumulation and Ablation Model (NWSRFS) use the depletion of SCA to predict liquid water (SWE) available for runoff using temperature index approaches. This approach was adopted into a physically based modeling framework by developing a relationship between the distribution of snow water equivalence over the basin, and the temporal dynamics of the areal extent of snowcover as discussed in the following manuscripts

Luce, Tarboton, and Cooley, 1999; Luce and Tarboton, 2004. They term this relationship depletion curve, not to be confused with previously described curves that relate snow covered area to accumulated degree days or temperature index approaches. Luce's suggested depletion curve, and the one presented here, may substitute for previously used depletion curves that use temperature index and/or degree-day approaches. In this study a depletion curve is defined as a graphical representation of snow depletion whose axes are fractional snow covered area (y-axis) and snow water equivalent (x-axis). I develop and display the curve in this way because I'm interested in deriving an equation that allows for predicting SWE based on the change in fractional snow cover over the duration of melt. The depletion curve itself is therefore a subgrid parameterization of snow variability.

Another way to quantify the variability of snowcover is with the use of probability distribution functions. Luce et al., 1999 showed that the shape of the depletion curve can be related to the cumulative distribution function and that the coefficient of variation (CV) is the most sensitive parameter. The CV can them be used as an estimate of the shape of the depletion curve because the SWE is normalized to the maximum SWE. Therefore the variability in snow can by parameterized by estimating coefficients of variation from the shape of the depletion curve.

Spaceborne instruments such as MODIS provide improved capabilities for repeat detection of snow at a resolution of 500 m. With the recent development of sub-pixel snow cover algorithms (Salomonson and Appel, 2004) with mean absolute error of less than 0.1 there is utility in incorporating estimates of fractional snow cover to more

accurately derive depletion curves. This method yields the fractional snow cover and helps to overcome the mixed-pixel coverage or partial coverage problems common with other snow-mapping techniques. This new approach for estimating snow cover from satellite imagery when incorporated into the depletion curve approach provides a new, more accurate, and transportable method for estimating the spatial distribution of snow and the relationship between snow water equivalence and snow covered area for use in hydrologic forecasting.

The purpose of this study is to determine if a depletion curve can be established in the Dry Creek Experimental Watershed using a distributed snowmelt model (Utah Energy Balance Snow Accumulation and Melt Model (UEB) to estimate SWE and repeated measurements of snow covered area from satellite imagery (MODIS) to estimate fractional snow covered area.

1.3 Background

Detailed snow surveys performed on a fine grid over a watershed basin have proven to be the most accurate way to represent the spatial distribution of SWE (Bloschl, 1999; Laydecker and Sickman, 1999). These methods however are costly, time consuming, and don't necessarily capture the variability of the depletion of snow during melt (Cline, Bales, and Dozier, 1998).

Remotely sensing snow has recently become a more appealing approach in addressing the issues of spatial and temporal variability (Koskinen, Pulliainen, and Hallikainen, 1997; Mote, Grundstein, Leathers, and Robinson, 2003; Swamy and Brivio,

1997). Distinctions can easily be made between land that is covered by snow and land that is not due to the reflectance signature of snow. Repeat measurements provide a time series of snow cover and therefore aid in the development of depletion curves used in snowmelt runoff models. This approach is appealing because it potentially eliminates the need for spatially distributed direct measurements. Several investigations have demonstrated the capability of using multifrequency microwave radiometer systems to locally map snow covered area, snow depth, and SWE (Koskinen et al., 1997). Through exploiting the spectral characteristics of snow, wet snow, and land without snow, these sensors can provide information on a scale of 30 m. These method however, are costly, have low return periods, and aren't readily available to researchers or operational forecasters. In addition, these methods have severe accuracy issues.

Moderate Resolution Imaging Spectroradiometer (MODIS) has a one-day return period and the images are provided free of charge thus making it appealing to researchers interested in collecting day-to-day snow information. Researchers at Goddard Space Flight Center have developed a fractional snow cover algorithm that allows for sub-pixel (<500 m) estimates of snow cover using MODIS imagery (Salomonson and Appel, 2004). This commonly used SNOWMAP algorithm has proven successful in mapping fractional SCA in a variety of different settings (Dery, Salomonson, Stieglitz, Hall and Appel, 2004). This method uses Landsat images as ground truth for estimating fractional SCA. Each 500 m MODIS pixel contains multiple 30m Landsat pixels. A binary classification of snow covered area is computed for the Landsat pixels within each MODIS pixel and a normalized difference snow index (NDSI) is computed for the

MODIS pixels. The data are linearly regressed and an expression is derived that relates NDSI to fractional SCA.

Snowmelt models to predict SWE have improved over the years, but accurate estimation requires simulating physical processes in a distributed fashion and usually requires weather data that is often unavailable. In an effort to minimize complicated calculations, but still drive research in the direction of an energy-balance physically based approach, modelers have relied on lumped parameter methods that predict spatially averaged snowmelt. These models have relied on degree-day methods and temperature index approaches to, at any give time during melt predict how much SWE remains in the snowpack (Dewalle, Henderson, and Rango, 2002; Martinec, Rango, and Roberts, 1999; Anderson, 1973). Because of their empirical approach, these methods often require multiple calibration parameters and may be limited to use catchments with site-specific characteristics.

A physically based accumulation and snowmelt model, called UEB (Utah Energy Balance Snow Accumulation and Melt Model) has provided support for use in a distributed fashion for a watershed in Southwest Idaho (Tarboton and Luce, 1996). Luce, et al., 1999 suggested the dimensionless depletion curve as a parameterization of subgrid variability in a physically based mass an energy balance snowmelt model. Luce related snow covered area to area-averaged snow water equivalent and produced a dimensionless depletion curve. Their methods for determining snow covered area involved intensive field surveys, while their methods for determining SWE involved intensive field surveys and snowmelt modeling using UEB. Their results showed that snow preferentially

accumulates in the same locations year after year and that a functional form of a deletion curve can be derived. The derived function can then be applied to other years.

Probability distribution functions are another approach for quantifying the spatial and temporal distribution of snow (Bloschl, 1999). The cumulative distribution function of the lognormal distribution has two parameters; standard deviation and mean, where the ratio of standard deviation to the mean is the coefficient of variation (CV). Taking the mean and standard deviation as equivalent, the cumulative distribution function varies based on the choice of the CV. Luce et al., 1999, Luce and Tarboton, 2004 papers suggested that the shape of a depletion curve can be fitted to the shape of the cumulative distribution function. Numerically, the x-axis' of the cumulative distribution function and cumulative melt normalized to the maximum cumulative melt are the same and range from 0 to 1. A value of 1 corresponds to a probability of 100%, and on the depletion curve corresponds to a fractional snow cover value of 100%. Therefore, once the depletion curve is established, a cumulative distribution function can be fit by the choice of the CV. In addition, Liston's work (Liston, 2005) supports this notion where subgrid snow-depth variability is parameterized using coefficients of variation given that snow has a lognormal distribution. Therefore, a depletion curve that characterizes the reduction of snow in terms of SCA and SWE can then be reduced to a single parameter (CV) for input into a hydrologic model.

1.4 Theory

In this study, a depletion curve is defined as a graphical representation of snow depletion whose axes are fractional snow covered area (y-axis) and snow water equivalent (x-axis). A functional relationship is derived that allows for the prediction of snow water equivalent (dependant variable) based on fractional snow covered area (independent variable). The advantage of this approach is that the curve describes the spatial pattern of snowmelt and that the depth of water entering the hillslope, driven by physical processes, is quantified by the functional relationship between snow covered area and the sum of a series of accumulated melt depths. Rather than using parameters to determine the onset of melt, and update a hydrologic model based on environmental conditions, the curve is dimensionless and can be used for different years. The basin average water equivalent (W_a) is represented by the sum of a series of thin layers (dw) as shown in Figure 1. The basin average snow water equivalent as a function of the accumulated melt is evaluated by the following:

$$W_a(M) = \int_M^{\infty} SCA_{af}(w)dw \tag{1}$$

where SCA_{af} is the fractional snow covered area, (w)dw is the change in modeled snow

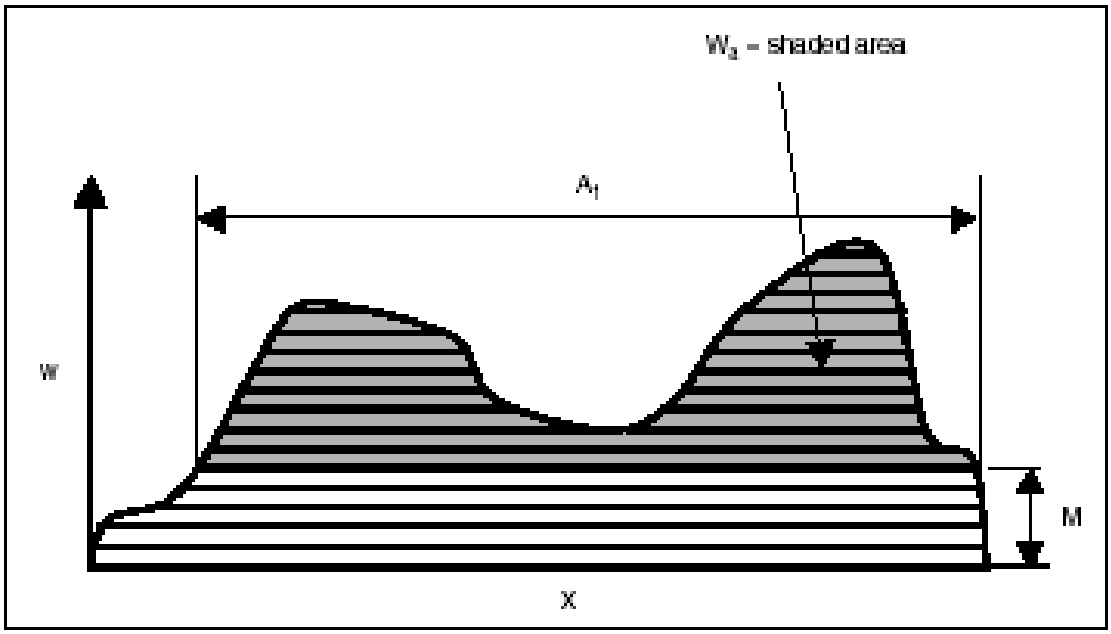

Figure 1. Schematic taken from Luce and Tarboton, 2004 showing that the basin water equivalent is represented by the sum of a series of melt depths.

water equivalence. This essentially distributes water equivalence to snow covered areas. A continuous function does not exist so the integral is approximated by the following summation:

$$W_a(M_i) = \sum_{j=i}^{n}\left[\frac{1}{2}(SCA_{af_{i-1}} - SCA_{af_i})\right] * (M_i) \tag{2}$$

This was accomplished for each element over each time step such that the sum of the elements at any given time represents the accumulated melt up to that point. The summation of all the 141 elements over each time step is calculated by:

$$W_a = \sum_{i=1}^{n}\left[\sum_{j=1}^{p}\left[\frac{1}{2}\left(SCA_{af_{i-1,j}} - SCA_{af_{i,j}}\right)\right] * \left(SWE_{md_{i,j}} - SWE_{md_{i-1,j}}\right)\right] \tag{3}$$

where n is the number of time steps, p is the number of elements, and SWE_{md} is the modeled snow water equivalence. Recognizing that the inverse of the accumulated melt is equal to the decrease in the basin snow water equivalent;

$$SCA_{af}(M) = 1 - \frac{W_a}{W_{a\max}} \tag{4}$$

Fractional SCA and SWE ($1-W_a/W_{amax}$) are plotted against each other to produce the basin depletion curve. By normalizing the SWE and expressing SCA as a fraction of the total area the two quantities can be plotted against one another so that the dimension of time is removed. This also accounts for the variability of snow year after year.

1.5 Project Description

This method builds on the results found by Luce et al, 1999 and Luce and Tarboton, 2004 for their study area in Southwestern Idaho. This research is advancement to current methods because the depletion curve is established using satellite imagery and a physically based energy and mass balance snowmelt model. It is an improvement to present day methods in 3 ways: 1) daily remotely sensed snow cover data, 2) accumulated melt is modeled only where there is snow cover, 3) derived equation and estimated CV's have a physical basis and can be used during successive years.

Specific objectives include: 1) obtain daily SCA measurements from MODIS using the universal regression approach. 2) model snowmelt in 1D for each MODIS pixel using UEB snowmelt model and distribute to snow covered areas, 3) derive an

equation that relates fractional SCA to SWE in the DCEW, 4) estimate coefficients of variation from the basin depletion curve and for unique zones within the basin.

2 STUDY SITE

2.1 Geographic Description

The Dry Creek Experimental Watershed (DCEW) is located in Southwestern Idaho approximately 16 km north of Boise Idaho (Figure 2). The DCEW encompasses a total area of 27 km^2 and is nestled in the foothills that are commonly referred to as the

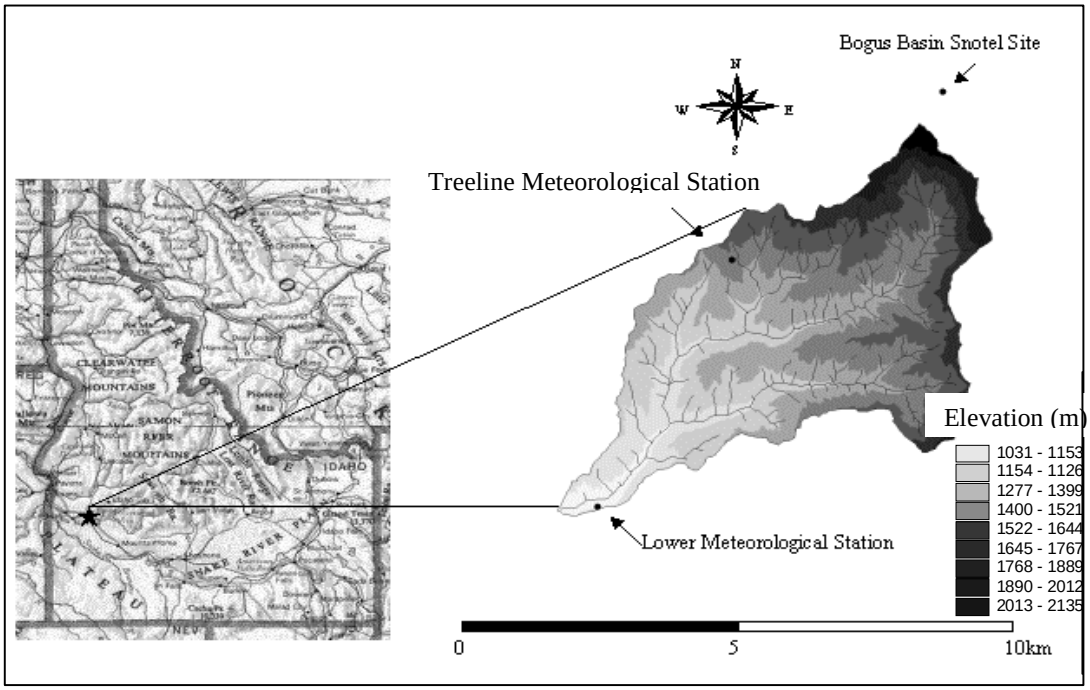

Figure 2. Location map of the Dry Creek Experimental Watershed. Also shown are the locations of three weather stations in and near the DCEW.

Boise Front. Bogus Basin Ski Resort is located nearby and the road to the resort allows for access to Dry Creek along its western edge. Bogus Basin Road Crosses Dry Creek at

UTM coordinates 4837309 northing, 566159 easting, (NAD27, Zone 11T) at an elevation of 1,029 m and defines the Southwestern most boundary of the DCEW. Its Northeastern most boundary and headwaters are located near Deer Point at UTM coordinates 4844801 northing, 572616 easting at an elevation of 2,139 m. The overall trend of the drainage basin is Southwest as it extends into the Treasure Valley and eventually flows into the Boise River. Dry Creek is a perennial stream within the DCEW with one perennial tributary, Shingle Creek, and numerous unnamed intermittent tributaries (Yenko, 2003).

2.2 Climate

Regionally, this area is described as a semi-arid climate but the complexity and variation in topography in the adjacent mountains results in considerable precipitation locally in the Boise Front and DCEW. Generally speaking, the winters are cold with precipitation falling primarily in the form of snow, while the summers are hot with occasional thunderstorms. Early springs are cool and rainy while late springs are sunny and warm. Falls are clear and warm changing to cold and moist (USDA , 1974).

The climate in this area occurs due to the convergence between the Aleutian Low and the Pacific High weather systems. The Aleutian Low bringing in cool moist air from the north near the Aleutian Islands and the Pacific High bringing in hot dry air from the south in the Pacific Ocean. The low-pressure system tends to dominate in the winter while the high-pressure system dominates in the summer (USDA, 1974).

There are three weather stations in and near the DCEW, one at the Lower Dry Creek Research Site, the second at the Treeline Dry Creek Research Site, and the third at

Bogus Basin Ski Resort (Figure 2). The Treeline and Lower weather stations are operated and maintained by the DCEW team while the Bogus Basin weather stations are run by Natural Resources Conservation Service (NRCS). These three weather stations are located at a range of elevations that are representative of the meteorological conditions occurring in this region. The weather stations have been operational for the following periods:

Lower Dry Creek: September, 1998 – Present

Treeline Dry Creek: September, 1998 – Present

Bogus Basin Snotel Site: May, 1999 – Present

2.3 Topography

The Geology of the DCEW consists primarily of granitic rock in a region that is tectonically inactive thus providing a setting for a dendritic drainage pattern with complex topography locally. Elevations in the basin range from about 1000 m to just over 2000 m over a distance of a few kilometers. Slopes are extremely variable ranging from 0° to 78° with the majority of the slopes between 56° and 62° and an average of 52.8°. The general trend of the Boise Front Range is south facing, and subsequently so is the DCEW, however aspects in the basin vary due to the dendritic nature of the topography. Aspects range from 0° to 360° clockwise from north with the majority of the values occurring between 226° and 236° with an average of 189.2°.

2.4 Vegetation

Vegetation in the DCEW varies as function of geology, topography, elevation,aspect, slope, and soil type. Of the entire watershed 82% (22.1 km^2) has been vegetation and land cover classified using landsat imagery. These Landsat derived vegetation maps are available though the USDA Forest Service, Boise National Forest and are products of the Wildlife Spatial Analysis Lab at the University of Montana (Redmond, Tady, Fisher, Thornton, and Winne, 1997). The area that has been mapped is coincidently at intermediate and upper elevations where vegetation and land cover exhibits the most variation (Figure 3).

Approximately 51% (11.27 km^2) is covered by Forestland while Shrublands cover

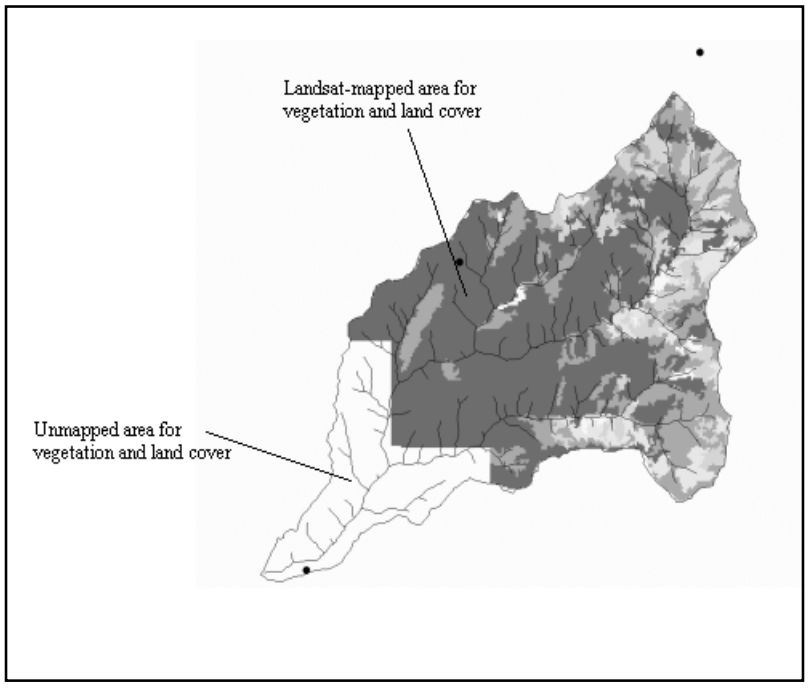

Figure 3. Map of the DCEW showing areas that have detailed information about vegetation and land cover.

about 40% (8.84 km^2). Grasslands and Barrenlands each make up 4% (0.88 km^2) and Riparian zones total an area 0.22 km^2 with 1% coverage. At lower elevations, where vegetation maps have not been produced grass and shrublands dominate with localized areas of barrenland and riparian. For the entire watershed, including unmapped areas, this effectively would reduce the percentage of Forestlands by about 7-9% since this area is below the treeline, and increase the percentages of shrublands by 7-9% due to the vast amount of Big Sagebrush Steppe. Table 1 summarizes these data with appropriate error bars on forestlands, shrublands, and grasslands. In terms of canopy cover values range from 1-100% coverage and is generally high at upper elevations where conifers dominate and low at lower elevations where shrublands dominate.

Table 1. Summary of the Dry Creek Experimental Watershed vegetation types as classified from Landsat Imagery

General Group	Percent coverage in the Watershed	Error (±)	Area in km^2	Parent Group	Sub-code Group	Percent coverage in the Watershed
GRASS-LANDS	**4%**	**2%**	**0.88**			
				Upland Grasslands		3.5%
					Altered Herbaceous	0.2%
					Mesic Montane Parklands and Subalpine Meadows	0.3%
SHRUB - LANDS	**40%**	**8%**	**8.84**			
				Mesic Shrubs		
					single or mixed species	12.5%
				Xeric Shrubs		
					Big Sagebrush Steppe	27.5%
FOREST-LANDS	**51%**	**8%**	**11.27**			
				Broadleaf Forest		
					Aspen	1.6%
				Conifer Forest		
					Ponderosa Pine	15.9%
					Douglas Fir	13.8%
					Douglas Fir/Lodgepole mix	0.4%
					Douglas Fir/Ponderosa Pine mix	15.4%
					mixed Xeric forest	0.2%
					mixed broadleaf and conifer	3.7%
RIPAR-IAN	**1%**	**1%**	**0.22**			
				Conifer dominated		0.5%
				mixed tree		0.1%
				Shrub dominated		0.4%
BARREN-LAND	**4%**	**2%**	**0.88**			4.0%
Total	**100%**		**22.10**			**100.0%**

2.5 Land Ownership

Approximately 42% (11.5 km^2) of the watershed is owned by the Boise National Forest and appropriately is located at upper elevations where douglas fir and ponderosa pine are of the greatest concentrations. The other 58% of the watershed is owned either by the Bureau of Land Management (BLM) (0.05 km^2), the State of Idaho (0.7 km^2), or private parties (15 km^2).

3 METHODS

The depletion of snow was determined using a distributed physically based snowmelt model to estimate SWE and using MODIS satellite imagery to obtain repeat measurements of fractional snow cover. Basin average fractional snow cover is plotted as a function of basin SWE to produce the DCEW depletion curve. The Utah Energy Balance Snow Accumulation and Melt Model was implemented in 1D and distributed to snow covered areas in 250,000 m^2 (500m x 500 m) elements. Fractional snow covered area in each element was estimated using the Universal Regression approach (Salomonson and Appel, 2004).

3.1 Watershed Delineation and UEB/MODIS Elements

The DCEW was delineated based on a 30m USGS DEM and divided up into 141 grid nodes corresponding to the centroids of the 141, 500 m resolution pixels observed by

MODIS (Figure 4). Each 250,000 m^2 area is designated as an element over which the UEB model is run and a SCA is determined from MODIS.

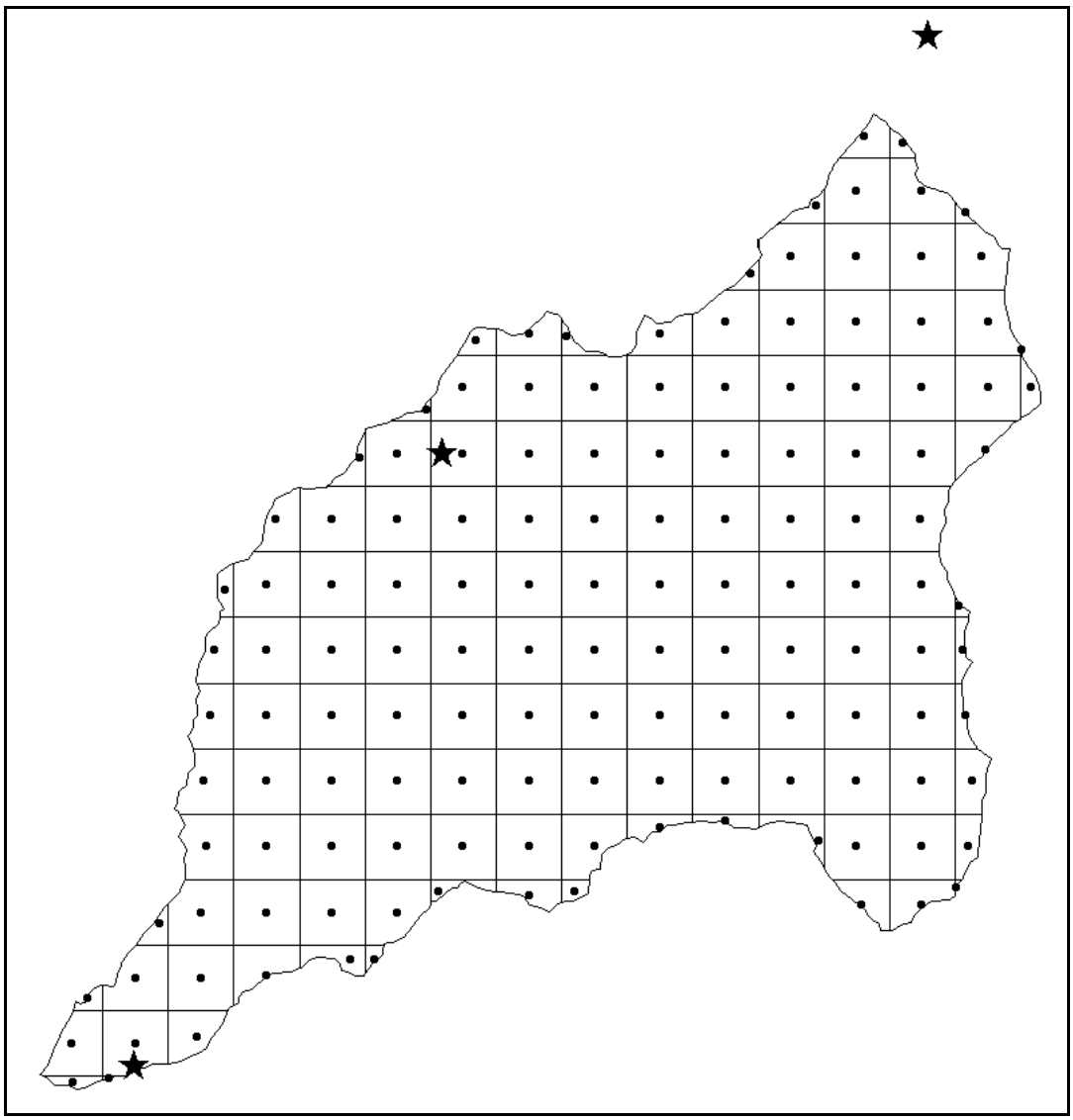

Figure 4. Model domain of the Dry Creek Experimental Watershed showing the locations of 141 MODIS elements and their respective centroids. Snowmelt was modeled at each centroid and distributed to those areas within the element that are snow covered. Stars show the location of three weather stations. Weather stations measure air temperature, precipitation rate, windspeed, relative humidity, and incoming shortwave radiation.

3.2 Utah Energy Balance Snow Accumulation and Melt Model (UEB)

UEB is a lumped parameter, semi-physically based model that characterizes the snowpack in terms of water equivalence and energy content relative to a reference state of water in ice phase at 0°C. Two primary state variables are maintained in the model, snow water equivalence, W [m], and internal energy of the snowpack and top 40 cm of soil, U [kJ/m^2]. U is zero when the snowpack is at 0° C and contains no liquid water. Appendix A contains a more detailed model description and a list of parameters used in the model.

UEB was initially designed to predict rapid melt rates responsible for erosion. The focus of the model therefore, is on the physical processes responsible for snowmelt, that is, energy exchanges at the snow-air interface. UEB was tested in the Reynolds Creek Experimental Watershed in Upper Sheep Creek Drainage, southeast Idaho, USU drainage and evapotranspiration research farm, Logan, Utah, and at Mammoth Mountain. These research sites are similar to the DCEW in terms of vegetation, terrain, and the dominant variables that affect snowpack heterogeneity.

Because melt outflow is a function of the liquid fraction the model can continue to transmit water to the soil even when the energy balance is negative. There are only three state variables (water equivalence, energy content, snow surface age) allowing the model to be easily distributed on a grid over a watershed thus making it very useful in hydrology studies. In addition, this parameterization simplifies computation and avoids having the model deal with complex processes that occur at the microscale within the snowpack.

3.2.1 Model Input Files

The main driving program calls to three input files that contain weather data, model specifications, and site characteristics. Those data are contained within the following files;

1. weather file
2. model parameter file
3. site variable file

1. The weather file consists of 5 temporal variables; air temperature, precipitation rate, wind speed, relative humidity, and incoming shortwave radiation.
2. The model parameter file consists of 30 fixed numerical parameters. These values are listed in Appendix A.
3. The site variable file consists of 8 site characteristics; forest cover fraction, drift factor, atmospheric pressure, ground heat flux, albedo extinction depth, slope, aspect, and elevation.

3.2.2 Meteorological Data

Five meteorological variables measured at three weather stations were used to compute the energy budget; air temperature, precipitation rate, windspeed, relative humidity, and incoming shortwave radiation. Precipitation was measured by weighing buckets mounted on posts at a height of 1.5 meters above ground. Windspeed was measured at a height of 2 meters above ground. Incoming shortwave radiation was measured using horizontally mounted pyranometers.

3.2.3 Distributing data to ungauged elements

All of the meteorological data was collected at hourly intervals and averaged over 6 hour time steps. Each meteorological variable was either distributed equally over the basin or was distributed by interpolating as a function of elevation as described below. The weather data was distributed to ungauged elements and compiled into 141 individual files that make up weather input files described above in Section 3.2.1. Because there are weather stations at representative locations in the watershed, variables such as temperature and precipitation are linearly dependant on the two nearest stations and are interpolated as a function of elevation. This eliminates the error associated with seasonal and diurnal fluctuations.

3.2.3.1 Air Temperature

Air temperature was distributed to ungauged elements between the treeline and Bogus Basin weather station by linearly interpolating between the two nearest stations.

There is very little or no difference in the air temperature measured at the lower weather station than that measured at the treeline weather station. Air temperature data from the treeline station was therefore distributed to all those elements equal to or less than the elevation of that weather station.

3.2.3.2 Precipitation

Precipitation rates were linearly interpolated as a function of elevation. Monthly average precipitation from four weather stations (Boise Airport, lower weather station, treeline weather station, and Bogus Snotel) were used to demonstrate that a linear

relationship exists between precipitation and elevation and therefore supports the method used here (Figure 5). 15 minute time series data of cumulative precipitation from treeline and lower weather stations are also shown in Figure 6. Increases in precipitation at lower weather station correspond to comparable increases at treeline station (Figure 5). The magnitudes of these increases are linearly related and demonstrate that precipitation can be interpolated as function of elevation. This relationship is similar for successive winter seasons and is assumed to exist for hourly, and therefore 6-hourly precipitation rates.

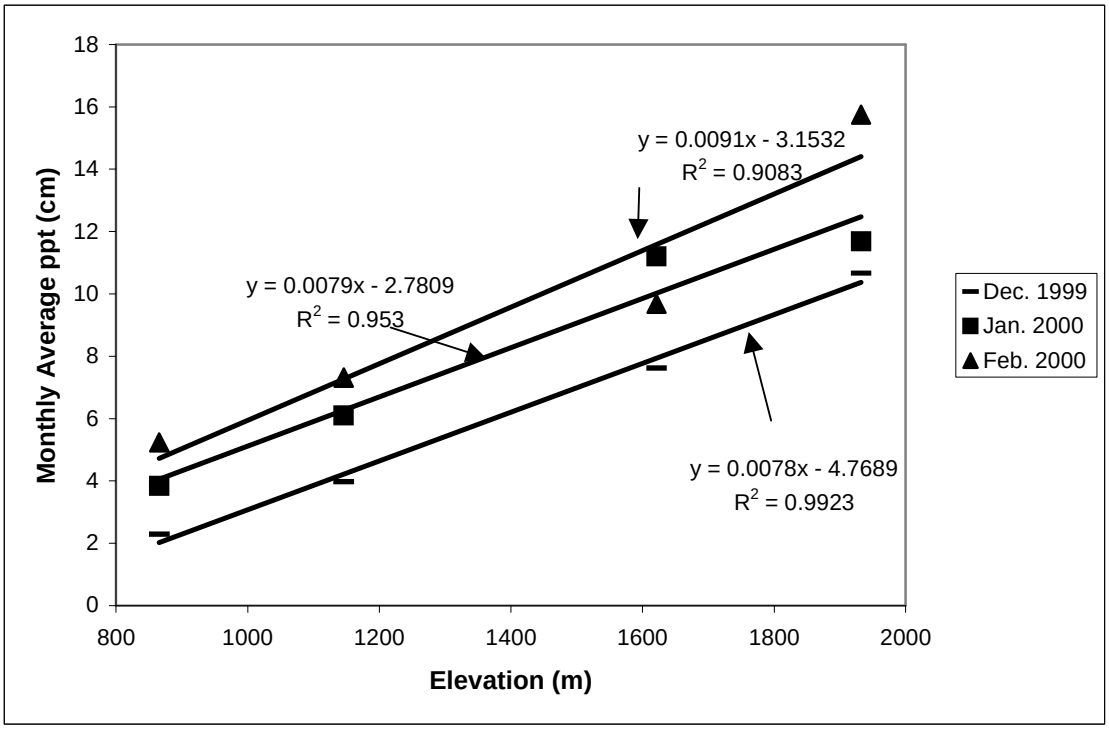

Figure 5. Precipitation rate versus elevation for the months of December 1999, January 2000, and February 2000 showing a linear relationship.

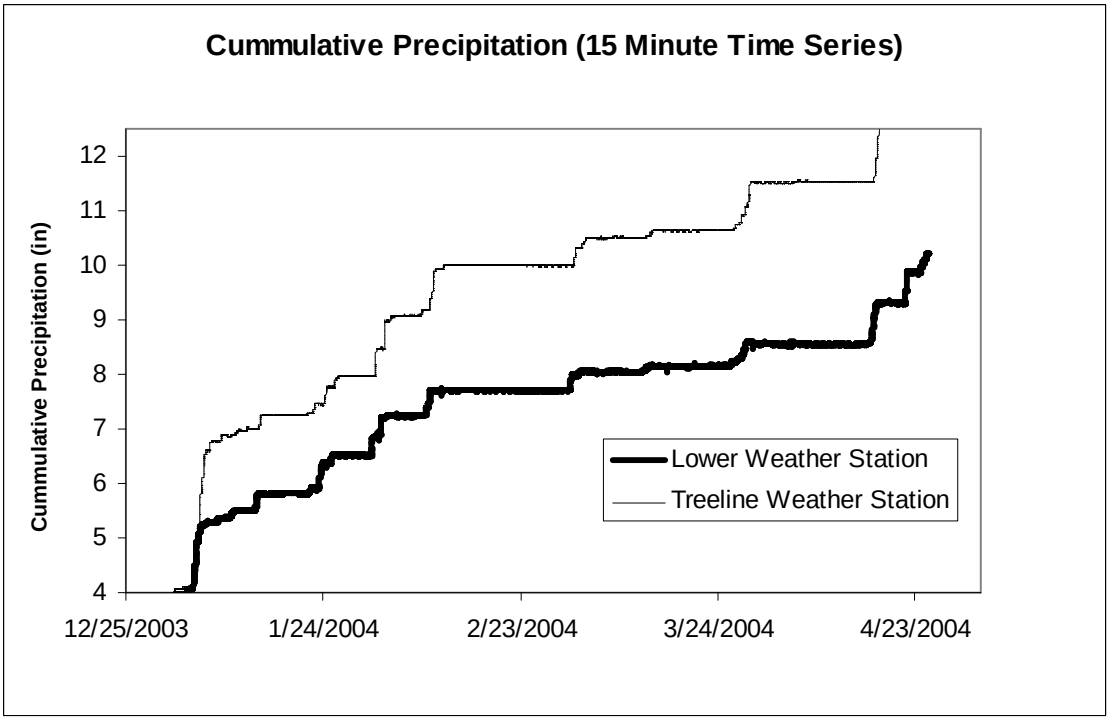

Figure 6. 15 minute time series of cumulative precipitation for treeline and lower weather stations. Increases in precipitation at lower weather station correspond to comparable increases at treeline station. The magnitudes of these increases are linearly related and demonstrate that precipitation can be interpolated between the two.

3.2.3.3 Windspeed

Windspeed was measured at a height of 2 meters above ground. Windspeeds are highly variable, are affected by local terrain features, and are notoriously difficult to estimate (Susong, Marks, and Garen, 1999). In the absence of other controls Susong et al., 1999 suggested elevation as the attributing factor responsible for the spatial variability of windspeed. I use this approach for distributing windspeed and interpolate as a function of elevation. I choose not to incorporate a physical wind model here because no information was available that allowed for assessment of the difference in

windspeed magnitude in valley bottoms versus ridgetops. However, averaging hourly data into 6-hour time steps dampened the effect of spiky data caused by wind gusts. The lower and treeline weather stations are positioned on topographically similar areas in terms of slope, aspect, and local terrain (on the edge of a ridge). This relationship exists between the treeline and Bogus Basin sites as well. Windspeed for elements at lower elevations were distributed by interpolating between the lower and treeline weather stations while those at higher elevations were distributed by interpolating between the treeline and Bogus Basin weather stations.

3.2.3.4 Relative Humidity

Relative Humidity was linearly interpolated as a function of elevation for ungauged lower elevation elements using lower and treeline weather stations and for higher elevation elements using the treeline and Bogus weather stations. To demonstrate that a linear relationship exists monthly average relative humidity values were linearly regressed against elevation (Figure 7). One-hour time series of relative humidity for treeline and Bogus stations are also shown in Figure 8. The plot illustrates that increases in the magnitude of relative humidity at mid elevation (treeline station) are comparable to increases in the magnitude of relative humidity at higher elevations (Bogus station). Since a comparable relationship exists for hourly data between two sites at varying elevation, and a linear relationship exists for monthly data between those sites it is determined that ungauged elements lying between them can be linearly interpolated.

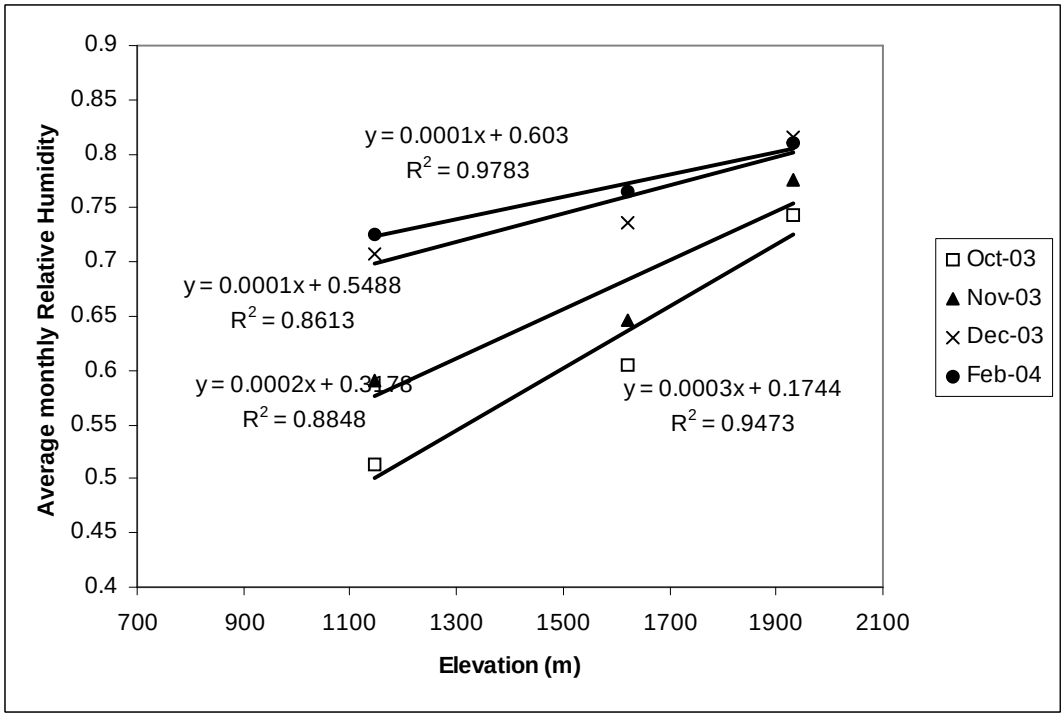

Figure 7. Relative humidity versus elevation for the months of January , February, and March 2000 showing the linear relationship.

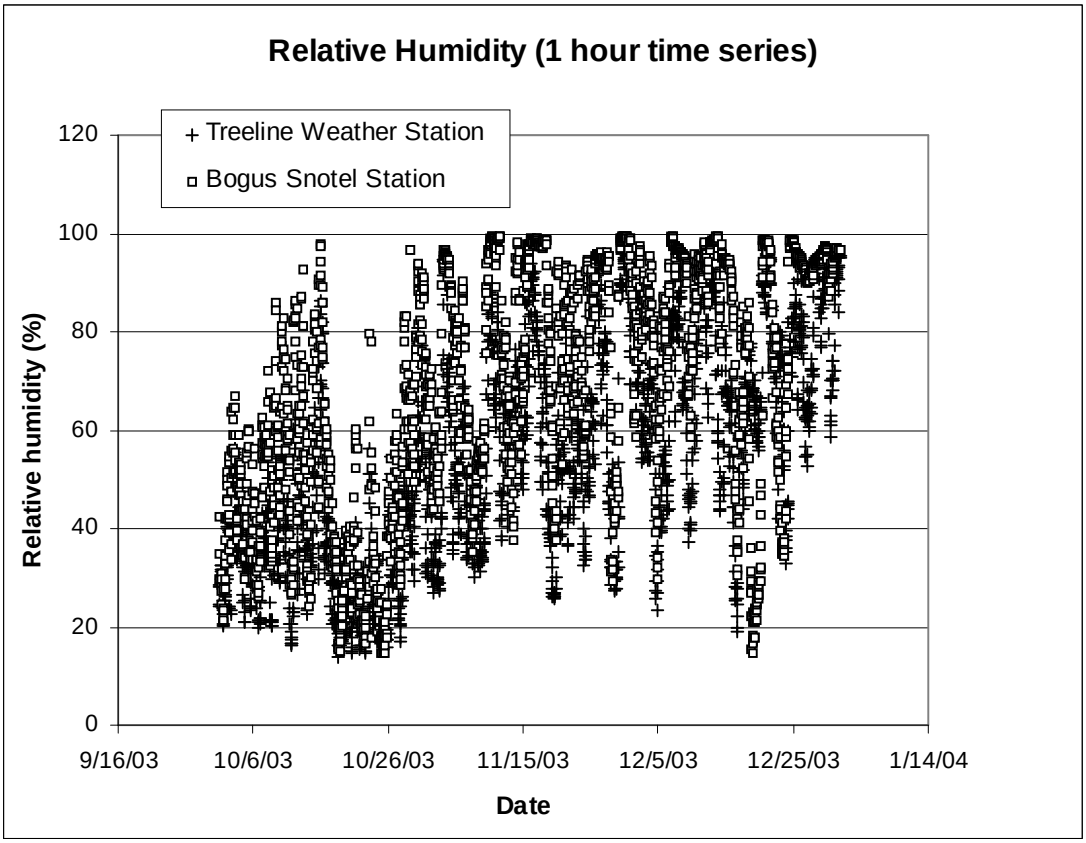

Figure 8. 1 hour time series of relative humidity for treeline and bogus snotel stations. The plot illustrates that increases in the magnitude of relative humidity at mid elevation (treeline station) are comparable to increases in the magnitude of relative humidity at higher elevations (Bogus station).

3.2.3.5 Solar Radiation

Clear-sky solar radiation was measured at three weather stations on horizontally mounted pyranometers. Solar radiation showed little or no variation between stations and therefore the values observed at the treeline station were distributed to all elements in the DCEW. In the UEB model albedo is calculated as a function of snow surface age and solar illumination angle following Dickinson, Henderson-Sellers, and Kennedy, 1993.

3.3 Site Variables

Each 250,000 m^2 area (element) was merged with a 30 m USGS DEM and average slopes, aspects, and elevations were calculated for each. This analysis was performed in ArcView GIS using the spatial analyst extension. These data were compiled into 141 individual files that served as the site variable files in the UEB model (discussed in Section 3.2.1. Forest cover fraction was determined from a Landsat-derived vegetation/canopy-cover map (Redmond, et al., 1997). Atmospheric pressure was linearly interpolated as function of elevation, ground heat flux was assumed to be negligible, and the albedo extinction depth remained at the default value of 0.1m as used in the Reynolds Creek Experimental Watershed study described in Tarboton and Luce, 1996. Due to the overall topographic trend of the watershed many south trending sub-drainages with accompanied west and east-facing slopes when averaged resulted in a south-facing slope. Because there is significantly more incoming solar radiation absorbed by the snowpack on south-facing slopes the artifact as a result of spatial averaging causes the UEB model to overpredict the actual energy content absorbed by the snow. This results in increased melting rates and inaccurate depletion results. To correct this problem, I converted the aspect grid from a range of 0°-360° to 0°-180°. In other words any slope from 0° to 180° remained the same while any aspect from 180°to 360° were differenced from 360° to give a complementary degree aspect within the range of 0°-180°. This method works under the assumption that the amount of average energy

received during the day, for example on a aspect of 90° is the same as the energy received by a aspect of 270°.

3.4 Model Verification and Comparison

No calibration was performed because the snowmelt model was only used to estimate the amount of melt between scenes. The amount of melt is accumulated up to the point in time when zero snow covered area is observed by MODIS. The time series of modeled SWE was compared to the time series of measured SWE at the nearby SNOTEL site (Bogus Basin weather station) for model verification. Furthermore, the modeled melt was compared to the DCEW hydrograph for additional verification.

3.4.1 SNOTEL Site

The UEB model was ran at the point corresponding to the location of the SNOTEL site at Bogus Basin Resort. This site is outside of the DCEW drainage, but was used to verify the reduction of SWE during the melt period.

3.4.2 Hydrograph

The results of the model were compared to the DCEW hydrograph. Total volume of event flow and effective input were computed. Response lags and lags to peak were computed for 4 distinct melt events.

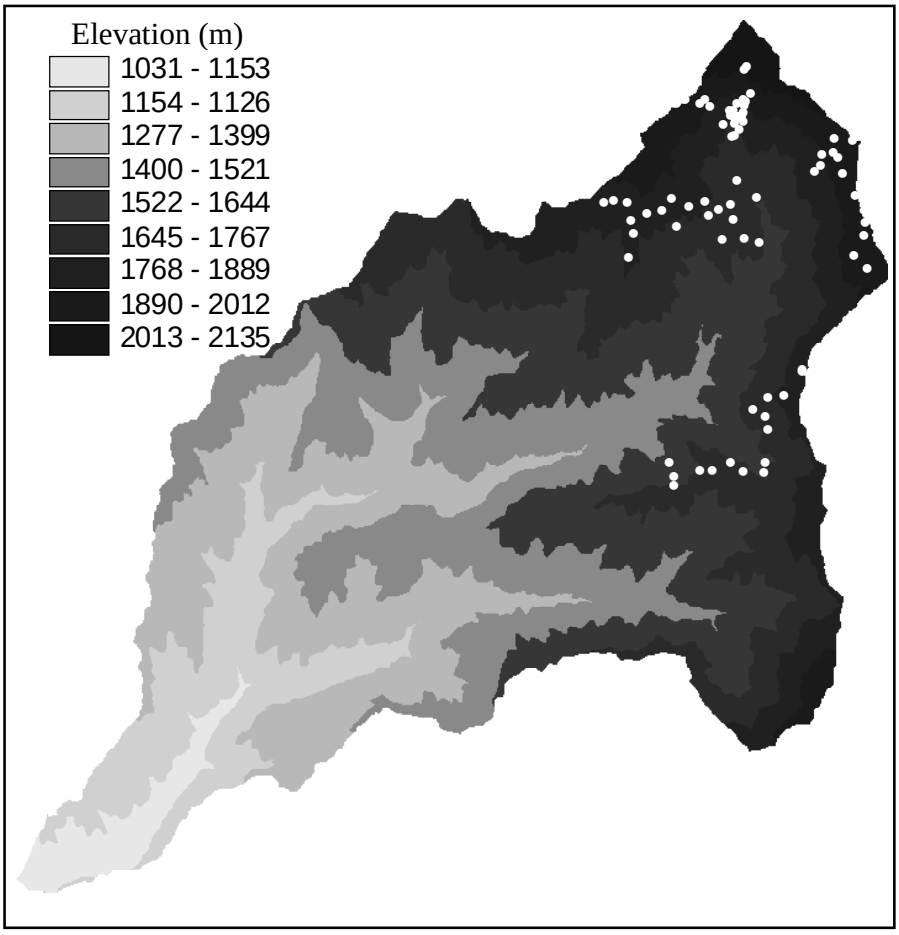

Figure 9. Map of the locations of snow samples taken with federal snow sampling tubes on March 27, 2004. Density, depth, and SWE were taken at each location.

3.4.3 Snow Survey

A snow survey was performed on March 27, 2004 with the intent to determine an average value for the basin SWE at maximum accumulation. Maximum accumulation occurred 3 weeks prior to the snow survey so alternatively, these data were used to verify methods for estimating coefficients of variation. Figure 9 shows the locations of sample locations.

Depth, density, and SWE measurements were taken with a Federal Snow Sampler. At each sample location 10 depth measurements were taken in about a 5 m diameter circle and within the circle 3 density measurements were taken. The average of these values was taken to be the true SWE.

3.5 MODIS Imagery

MODIS or Moderate Resolution Digital Spectroradiometer is aboard the EOS Terra and EOS Aqua satellites. A complete description can be found at MODIS's homepage at http://modis.gsfc.nasa.gov/. MODIS has a 1-day return period and has 36 spectral bands. MODIS images were acquired on a daily basis during the months of October 2003, through May 2004. MODIS images used were the Level 1b MOD02 calibrated radiances at 500 m resolutions. Data was downloaded from EOS data gateway: http://edcimswww.cr.usgs.gov/pub/imswelcome/. Only images that were cloud free were used in this study.

3.5.1 Fractional Snow Covered Area from MODIS

Snow covered areas are easily distinguished from snow free areas because of the spectral signature of snow. Snow has high reflectance in the visible portion of the spectrum and low reflectance in the shortwave infrared portion of the spectrum. Therefore, Landsat's bands 2 and 4 and MODIS's bands 4 and 6 can exploit this signature.

The method for determining fractional snow cover (SCA_{af}) was developed by researchers at NASA/Goddard Space Flight Center (Salomonson and Appel, 2004). Justin Huntington at Desert Research Institute performed the image processing and application of this method.

SCA_{af} (fractional snow covered area) was determined in the DCEW by using the following universal regression approach as described in Salomonson and Appel, 2004:

$$SCA_{af} = 0.06 + 1.21 * NDSI \tag{5}$$

The NDSI is an intensity of reflectance's that yields information about the area within a MODIS pixel that is covered by snow. NDSI is index of the snowcover and therefore an estimate of the SCA_{af} is made. Enhanced Landsat Thematic Mapper-Plus (ETM+) was used for groundtruthing. The universal equation above is a result of the linear regression between groundtruth SCA_{af} as determined from Landsat imagery, and NDSI as determined from MODIS imagery. The NDSI equation is as follows:

$$NDSI = \frac{band4 - band6}{band4 + band6} \tag{6}$$

where band4 and band6 are the at observed at-satellite reflectance's. MODIS reflectance pixels were clipped to the boundary of the DCEW and NDSI was determined for each element. NDSI pixel values were then applied to the universal equation to determine daily SCA_{af} for each pixel for the study period.

3.6 Depletion Curve

Depletion curves were established for the entire basin as well as higher elevation, intermediate elevation, and lower elevation zones following the procedure described in Section 1.4. Similarity exists between the depletion curves of individual elements in three unique zones. Generally, higher, intermediate and lower elevation elements were independently unique and therefore subdivided. The elevation band between 6025' and 6800' corresponds to the higher elevation zone, 4475'- 6025' to the intermediate elevation zone, and 3700'- 4475' to the lower elevation zone. Depletion curves were also established for individual elements corresponding to areas where snow survey data was recorded.

3.7 Coefficients of Variation

Coefficients of variation were estimated for the basin depletion curve, lower, intermediate, and upper elevation depletion curves. The cumulative distribution function of the log-normal distribution was visually fitted to each depletion curve on a trial-error basis by the choice of the coefficient of variation. The mean remains at one and standard

deviation is equal to the coefficient of variation. Because the x-axis of the depletion curves are expressed as ratio of the SWE to the maximum SWE observed then the cumulative distribution function of the log-normal distribution can be directly fitted.

The method for estimating coefficients of variation was tested/verified by comparing element depletion curves to snow survey data. A depletion curve was established for each element that had snow survey data following the method described above. From the snow survey data a CV was calculated in each of these elements by the following:

$$CV = \frac{S\tan dardDeviation}{Mean} \tag{7}$$

OR

$$CV = \frac{\sqrt{\frac{n\sum x^2 - \left(\sum x\right)^2}{n(n-1)}}}{\frac{\sum x}{n}} \tag{8}$$

where n is the number of samples, and x is the sampled SWE. Figure 10 shows the location of the snow samples (red dots) and corresponding element numbers. Element numbers 3, 10, 15, 16, and 17 were used.

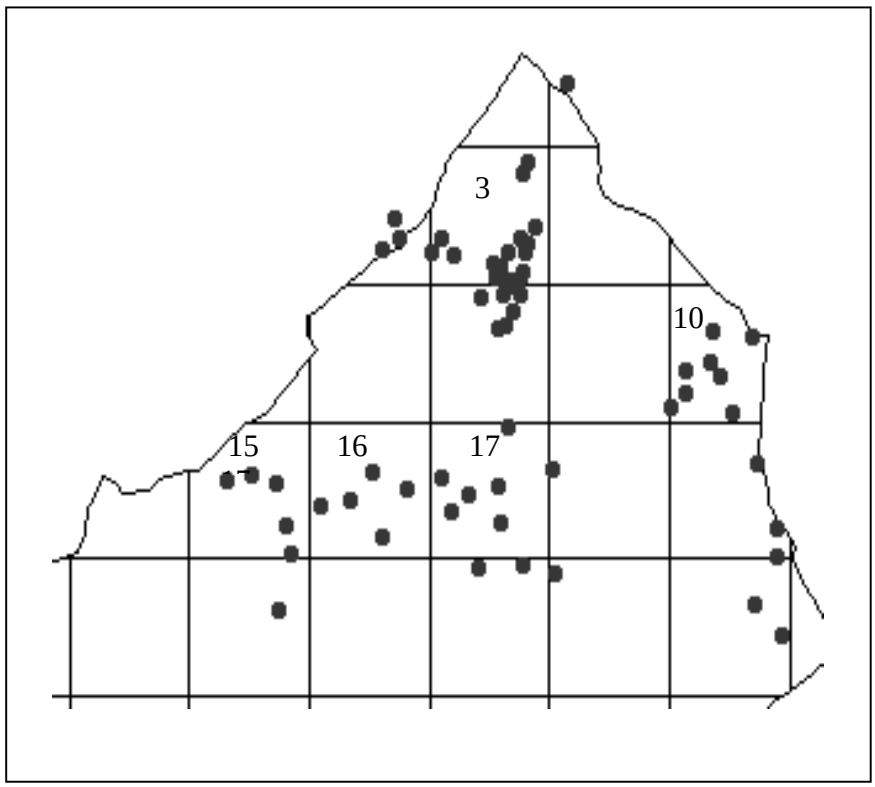

Figure 10. Map of higher elevation elements where snow survey was performed on March 27th, 2004. The elements are labeled by their corresponding ID number and delineated by each 500 m^2 box. Snow Survey data was used to calculate coefficients of variation and compare them to estimated CV's from element depletion curves.

4 RESULTS AND DISCUSSION

4.1 Model Verification

The UEB model performed well in predicting the accumulation and reduction of snow water equivalent values when compared to measured values at Bogus Snotel Site. The time series of modeled SWE (solid line) and measured SWE (dashed line) are shown

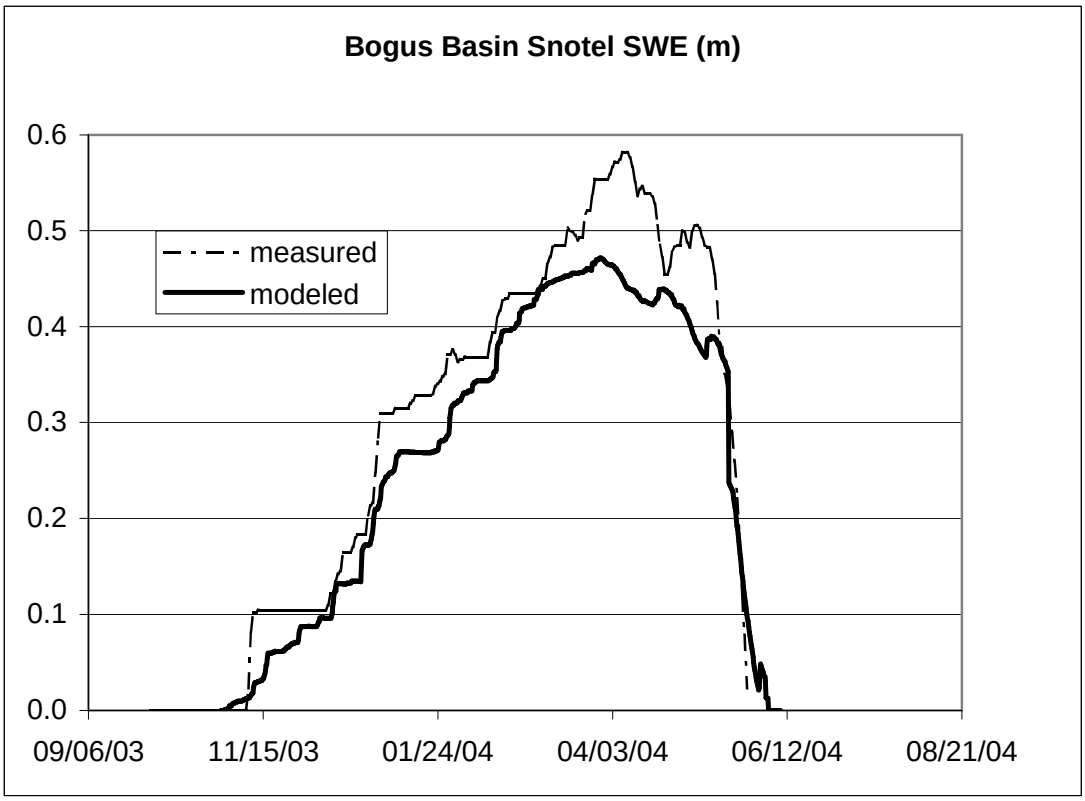

Figure 11. Time series of modeled SWE (solid line) and measured SWE (dashed line) at the Bogus Basin Snotel Site. The peak SWE value of 0.58 was not well simulated but the melt dynamics are well captured thus verifying the method of using modeled accumulated melt to derive the depletion curve.

in Figure 11. The model did not accurately simulate the measured peak SWE value of 0.58 m compared to modeled peak SWE value of 0.47 m, but performed exceptional at predicting the change in SWE between scenes. This suggests that the melt dynamics are well simulated and therefore verify the approach of using UEB to estimate the accumulated melt used in deriving a depletion curve.

4.2 Element depletion curves

The time series of SCA_{af} and SWE_{md} are used to develop each depletion curve. Figure 12 shows the results of a typical time series. Similar to the computation in equation 2, these data are used to develop the corresponding depletion curve for that particular element. The elements are then summed over the entire basin to produce the basin depletion curve (Section 4.4).

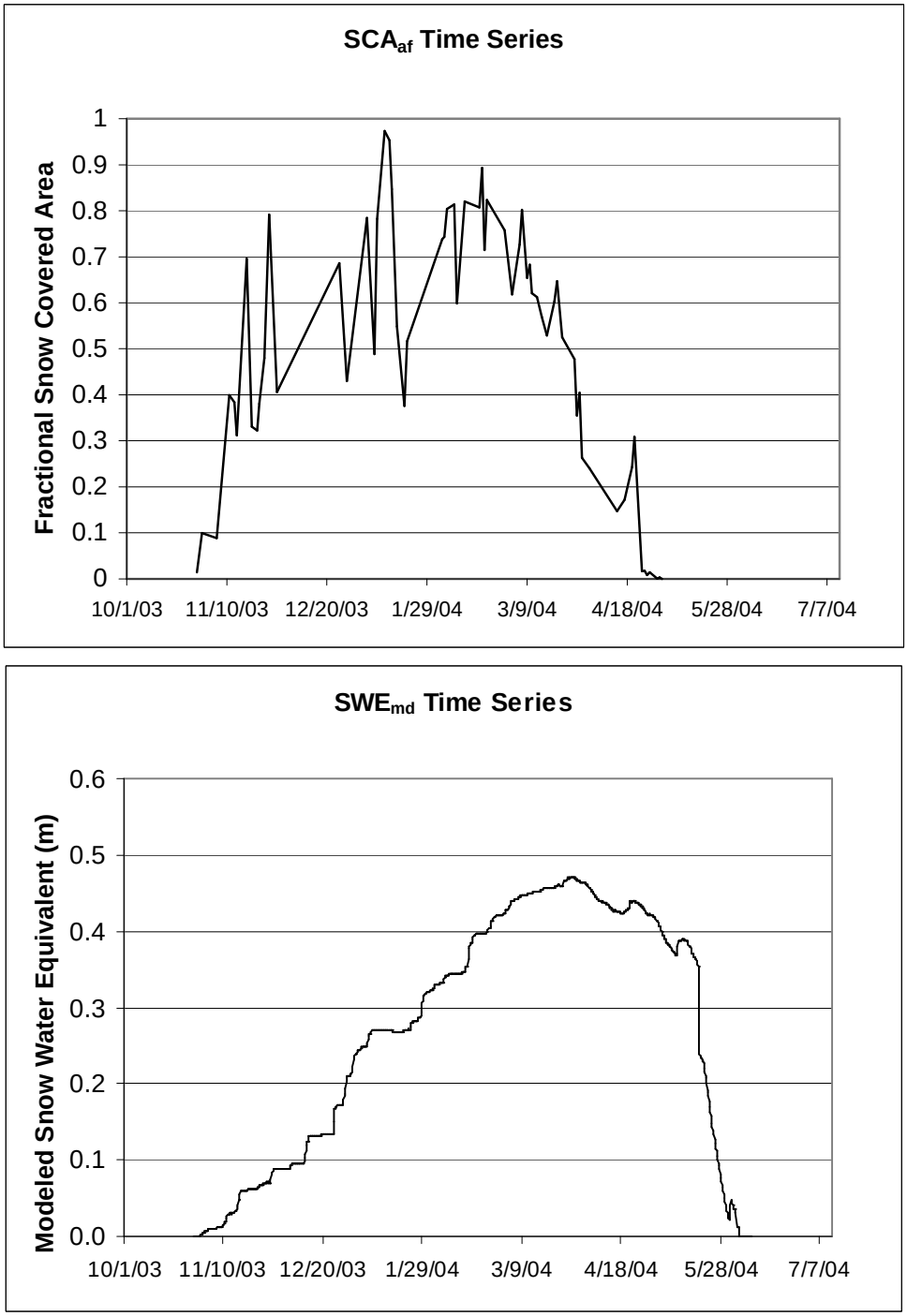

Figure 12. Time series of SCAaf (top) and SWEmd (bottom) of a typical model element. These data are used to derive a depletion curve. The elements are summed over the entire basin to produce the basin depletion curve.

Those elements located at lower elevations accumulate considerably less snow than those at higher elevations and the rate at which snow depletes at lower elevations is much greater than that at higher elevations. Individual element depletion curves are therefore summarized by three zones of which similarity exists within those zones; high elevation depletion curves (1836-2072m), intermediate elevation depletion curves (1364-1835m) and lower elevation depletion curves (1127-1363m). Curves are shown in s 13, 14, and 15. The date at which maximum SWE occurs for the 141 elements varies between January 29, 2004 and March 11, 2004. Generally, the more total snow that is accumulated (high elevation zones) the later in time that maximum SWE occurs for those elements and the less snow that is accumulated (low elevation zones) the earlier in time that maximum SWE occurs. This generalization is qualitative and serves as the basis for displaying the more than 7,000 data summarized into three zones.

The general shape of each depletion curve yields information about the spatial and temporal distribution of snow across the DCEW. Higher elevation curves (Figure 13) are typically sigmoidal in shape where decreases in SWE are observed but fractional snow cover remains somewhat constant at the onset of melt. As the snow continues to melt decreases in fractional snow cover are observed and occur at an increased rate. Molotch, Panter, Collee, others, (2001) showed similar trends for the Tokopah Basin, Sierra Nevadas. They attribute this to the depletion of snow primarily in the vertical direction followed by decreases in the horizontal direction. There is no evidence that would suggest that snow preferentially depletes in either the vertical or horizontal direction, however, I believe these results indicate that for higher elevations there is some critical

depth, below which fractional snow cover area is the dominate variable. The snowpack in these elements are reduced up to 30% before a reduction in SCA is observed. This is attributed to patchy snowcover due to redistribution by wind such that there are shallow and deep areas of accumulation. This is confirmed by field observations of drifting along the leeward slope and scouring occurring along ridge tops.

Intermediate elevation curves (Figure 14) show that there is an immediate decrease in SCA and an immediate decrease in SWE at the onset of melt. The slope of the curve shows that the rate at which SWE is decreasing is greater than the rate at which SCA is decreasing. This implies that fractional snow cover influences the distribution of snow but that the reduction of snow is dominated by the SWE variable. Lower elevation depletion (Figure 15) curves are nearly a straight line indicating that SCA and SWE are depleting at proportional rates. At the onset of melt there is an immediate decrease in SCA followed by a rapid melt event where nearly 80% of the SWE is melted. It is likely that the snowpack has a bimodal distribution where large areas are covered by a thin layer of snow, and the remaining areas are more localized and deeper. The initial melt uncovers the thin areas, thus dramatically decreasing SCA without significantly changing SWE. This event is then followed by the melt of the more localized deeper snow thus SCA and SWE decrease proportionally. Because of the large gaps in data any curve fit to the data points may have considerable inaccuracy. More discussion follows in the coefficients of variation Section (4.4).

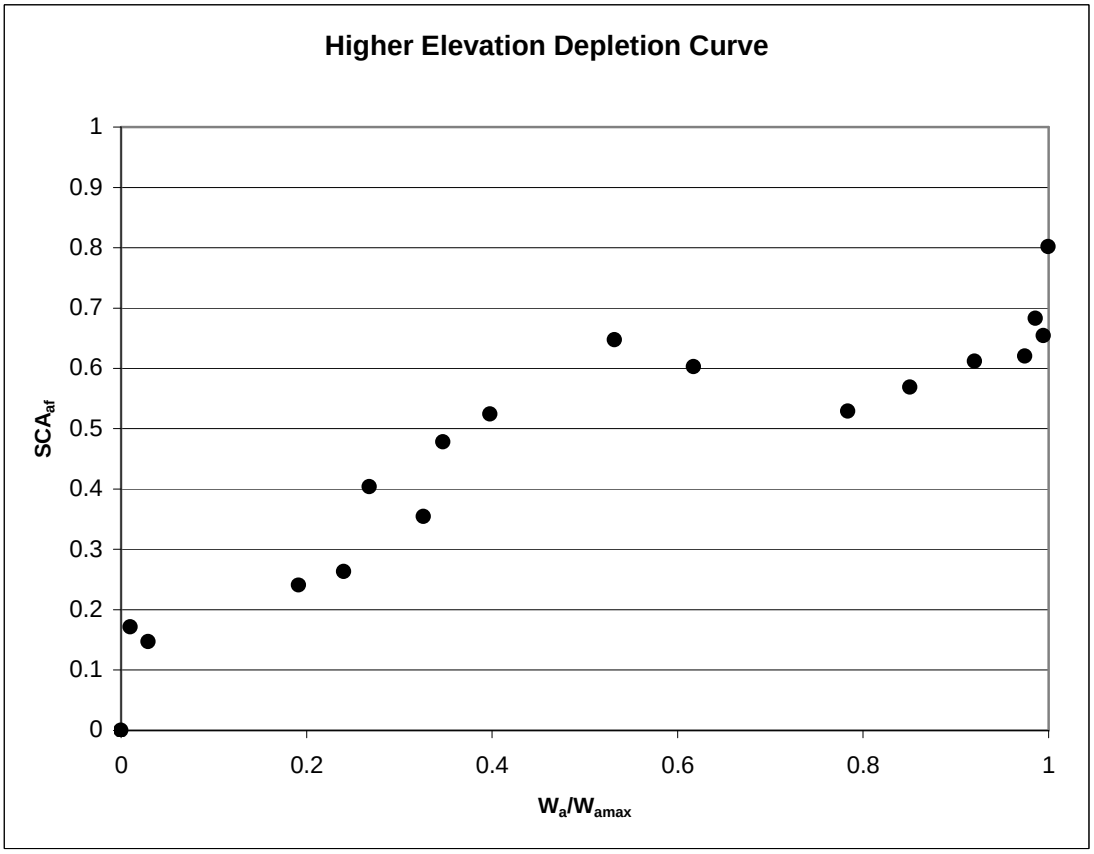

Figure 13. Depletion curve for higher elevation elements (1836-2072m). At the onset of melt there is very little change in the SCA. As melt progresses SCA decreases at a greater rate than SWE indicating that there is some critical depth below which SCA is the dominate variable.

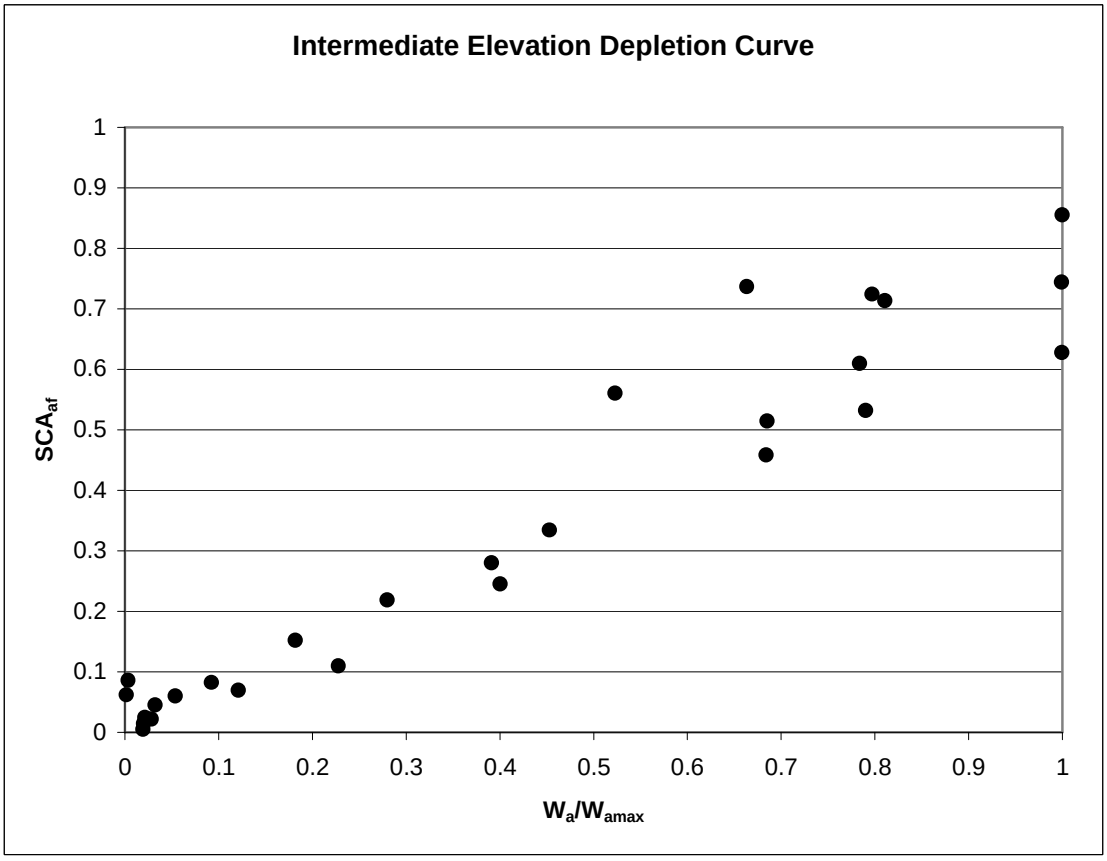

Figure 14. Depletion curve for the intermediate elevation elements (1364-1835m). At the onset of melt there is an immediate decrease in SCA and SWE. SWE decreases more rapidly than SCA does over the duration of melt and suggests that SCA is not a limiting variable in quantifying the depletion of snow for intermediate elevations.

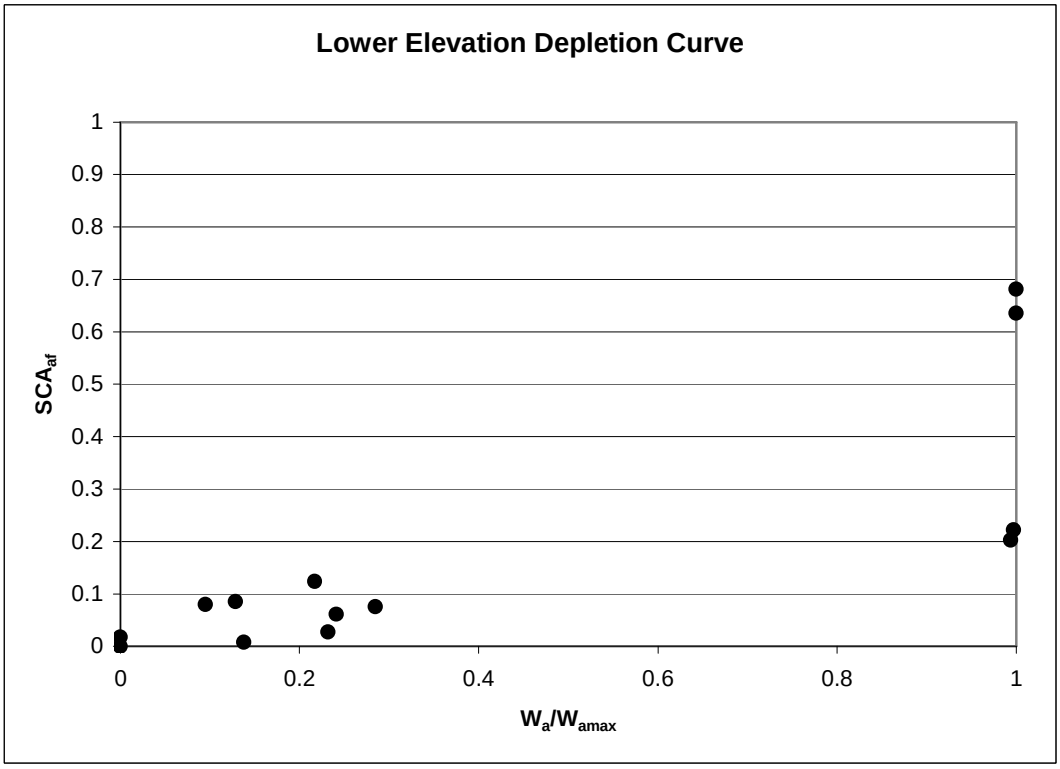

Figure 15. Depletion curve for lower elevation elements (1127-1363m). At the onset of melt there is an immediate decrease in SWE and an immediate decrease in SCA. This is followed by an extreme melt event where SWE decreases rapidly by nearly 80%. The lack of data within this area results in significant inaccuracy in a derived depletion curve equation or estimated CV.

4.3 SWE and SCA distribution

Well after snow has completely melted at lower elevations, upper elevations continued to accumulate snow. As UEB output and MODIS satellite imagery suggests, SWE and SCA are distributed differentially across the DCEW. These data are displayed in the following three map view illustrations (Figures 16 through 21). The SWE values shown are only for visual display of the spatial heterogeneity and do not represent physically real water equivalence values. Since the melt is calculated by the incremental change in modeled SWE these data are not used directly to establish the depletion curve.

Three dates were chosen to display these results; February 22nd where 30% of the elements have reached max accumulation, March 7th where 56% of the elements have reached maximum accumulation and subsequently the other 44% have already been melting for nearly 20 days, and April 17th where only elements at higher elevations have snow. In general, higher elevation, north facing slopes have higher associated SWE values while lower elevation, south facing slopes have lower SWE values.

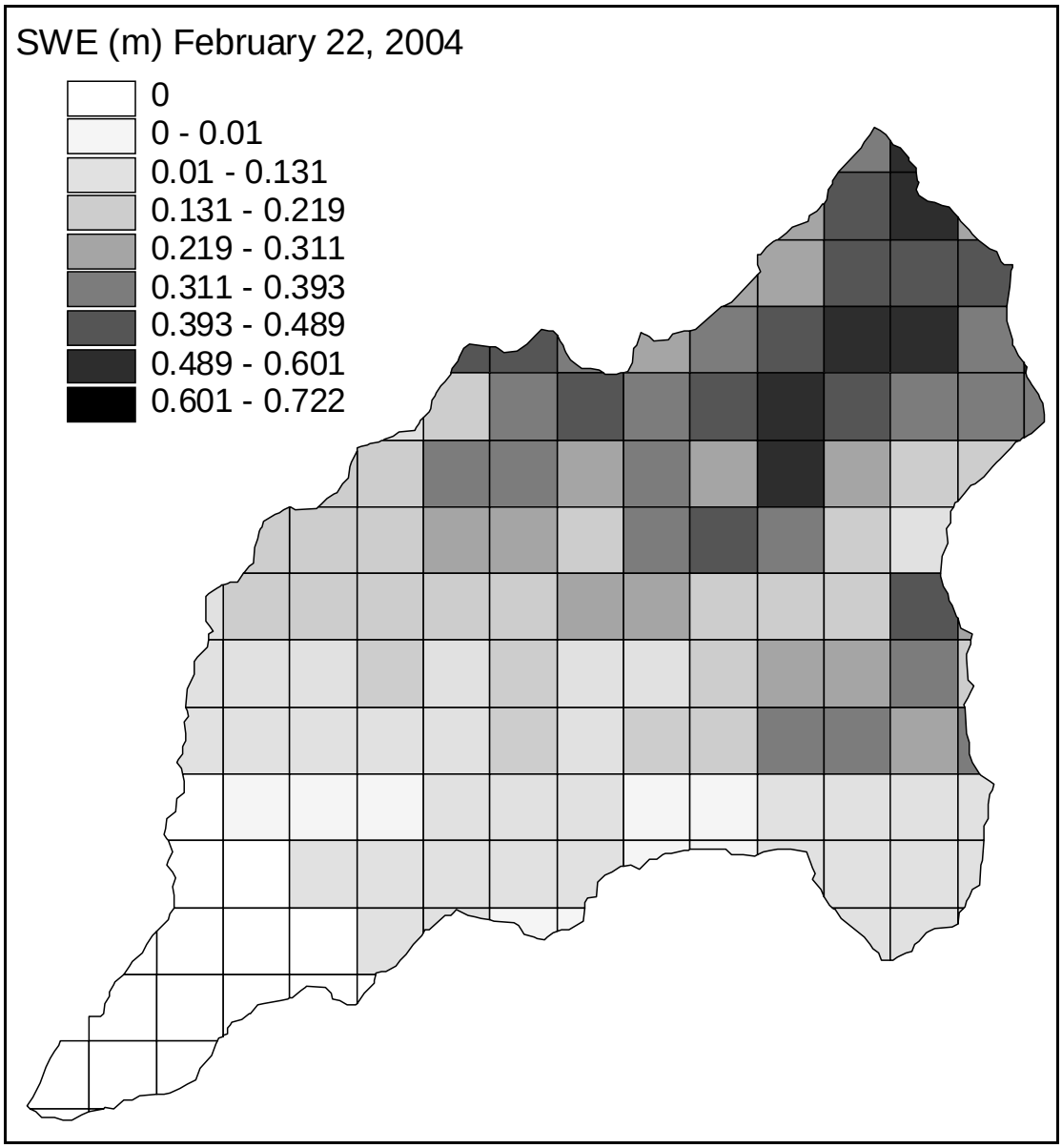

Figure 16. SWE distribution on February 22, 2004. Higher elevation, north facing elements have higher SWE values during accumulation early in the season. SWE values are displayed by a gray color ramp ranging from from 0 m to 0.722 m 0 being white, and 0.722 being black.

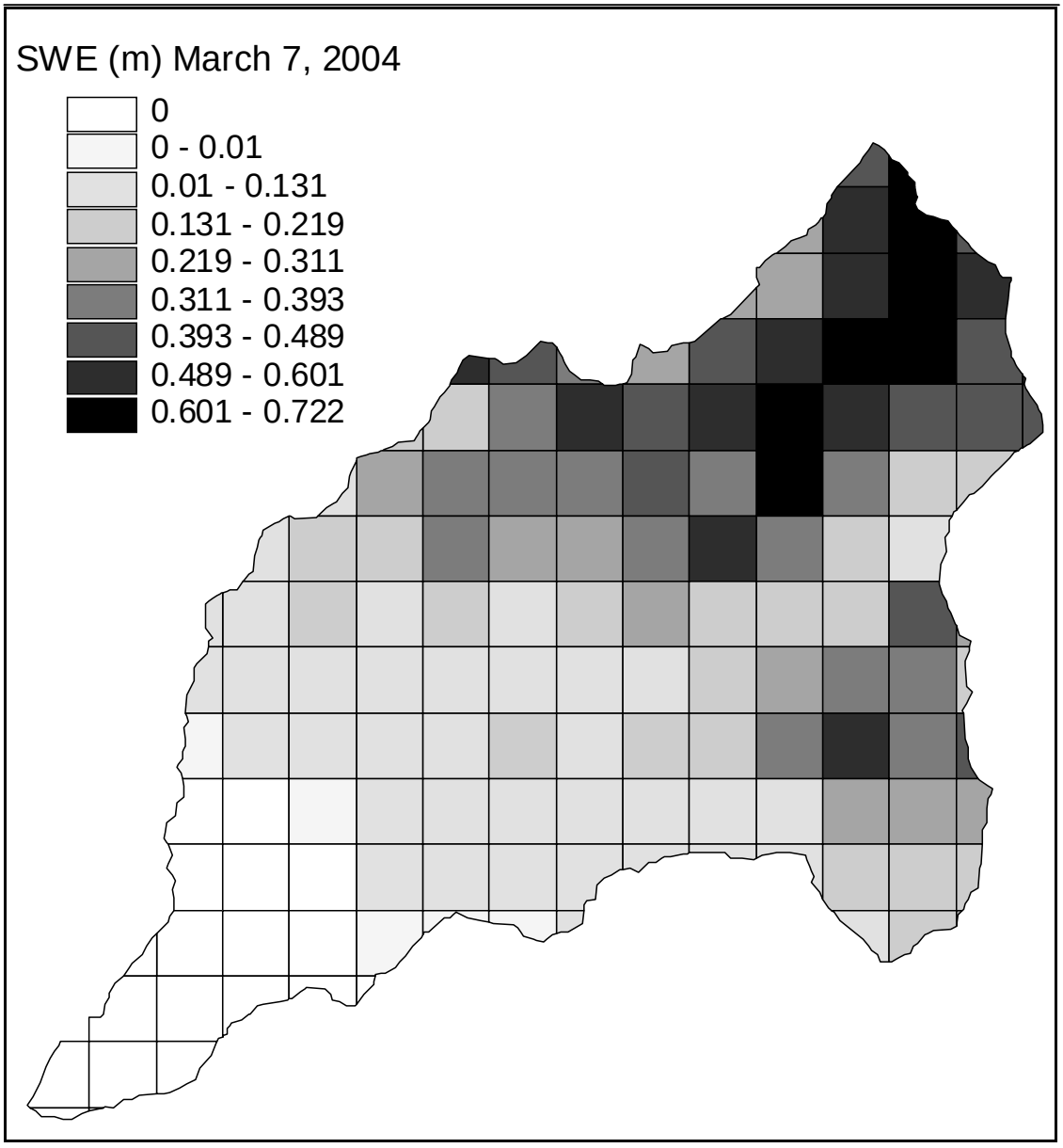

Figure 17. SWE distribution at basin average maximum accumulation (March 7, 2004). SWE values are displayed by a gray color ramp ranging from from 0 m to 0.722 m 0 being white, and 0.722 being black. At max accumulation elements below 1310m in elevation have zero snow, while higher elevation, north facing elements have considerable snow.

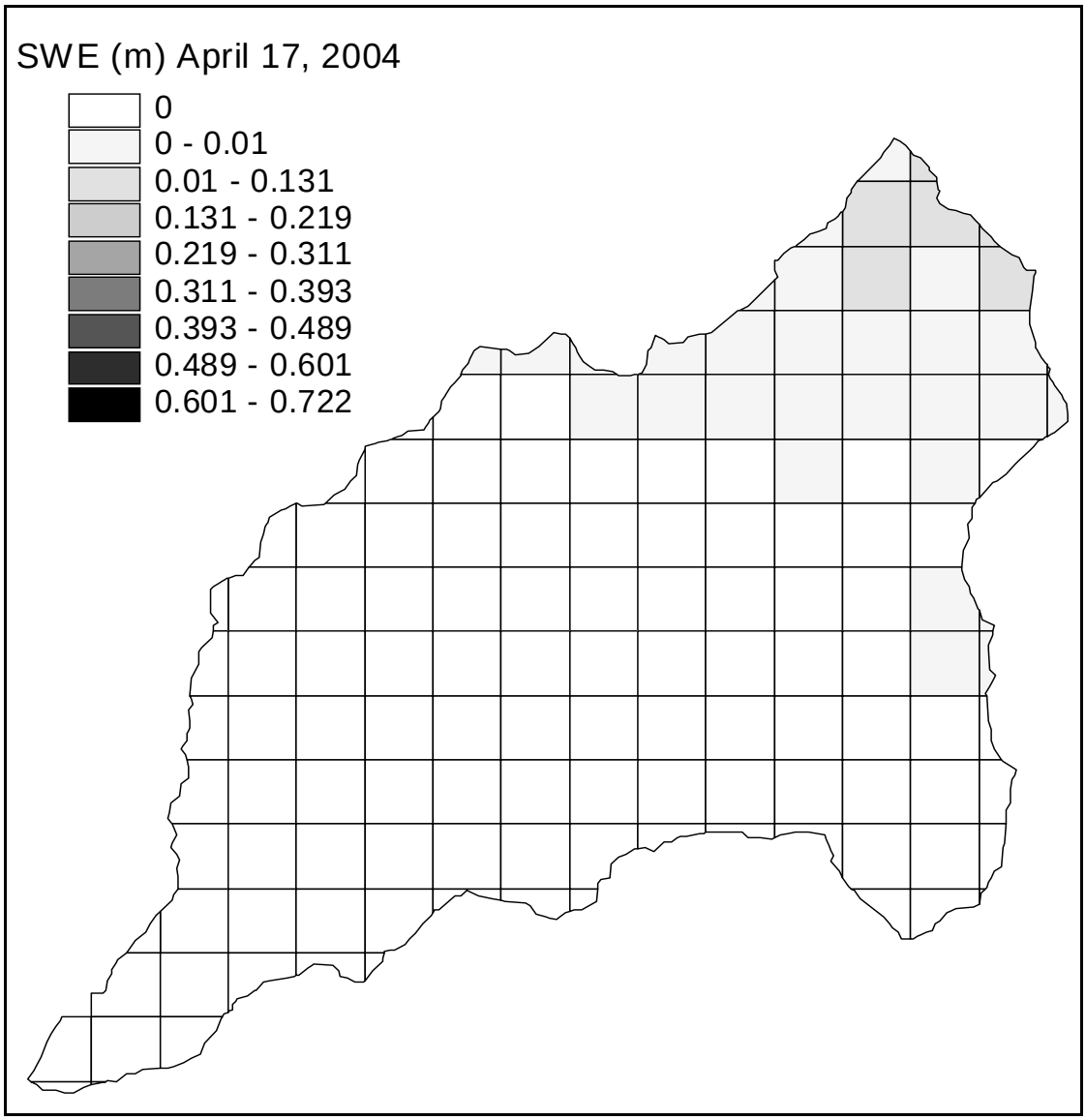

Figure 18. SWE values are displayed by a gray color ramp ranging from from 0 m to 0.722 m 0 being white, and 0.722 being black. All elements exept those at higher elevation, north facing slopes have zero snow.

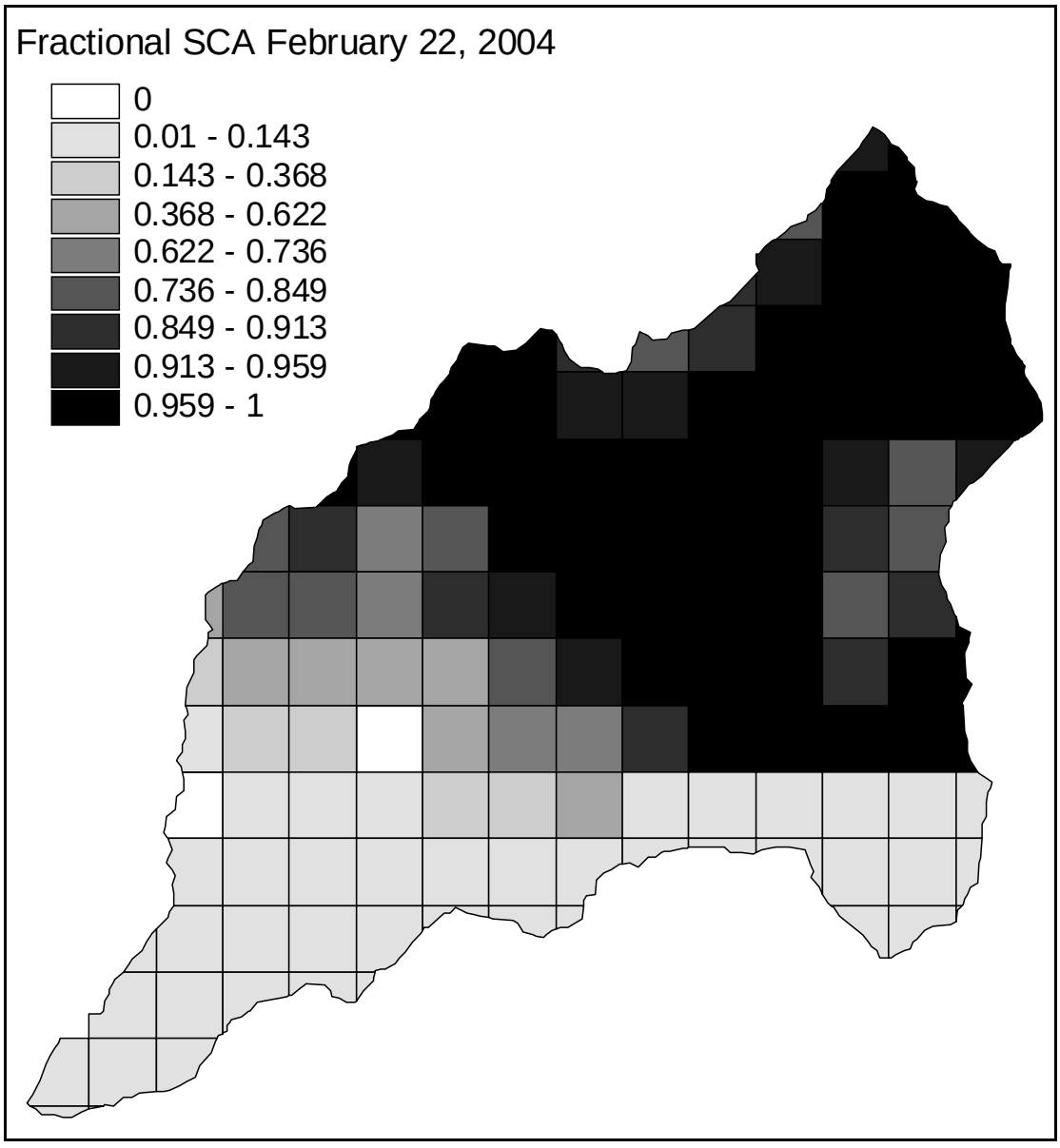

Figure 19. SCA values are displayed by a gray color ramp ranging from from 0 m to 1, 0 being white, and 1 being black. Snow cover is 100% for nearly all of the higher elevation elements.

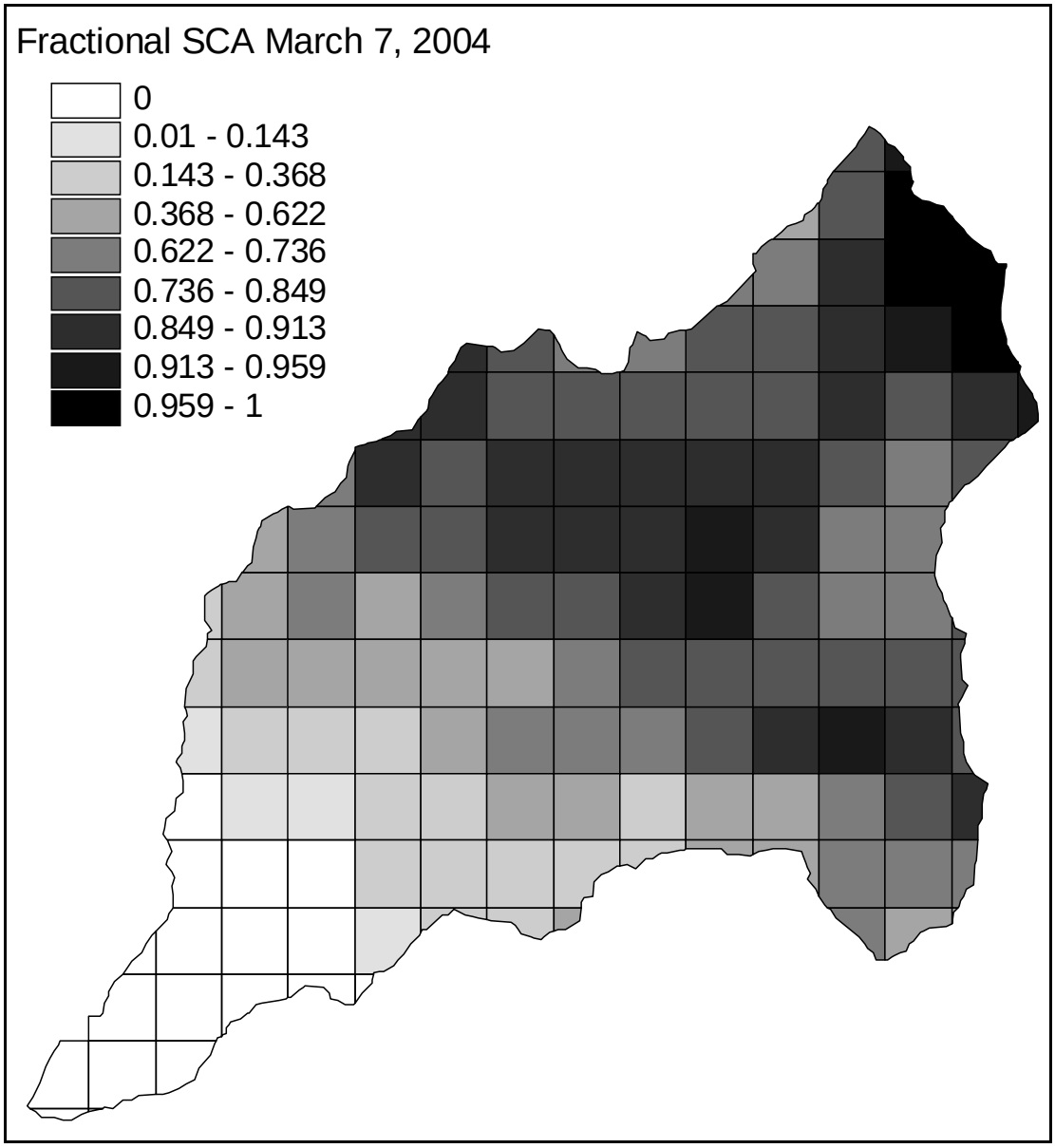

Figure 20. SCA values are displayed by a gray color ramp ranging from from 0 m to 1, 0 being white, and 1 being black. Elements at lower elevations are snow-free while elements at higher elevations and in close proximity to the main channel are between 70 and 100% snow covered.

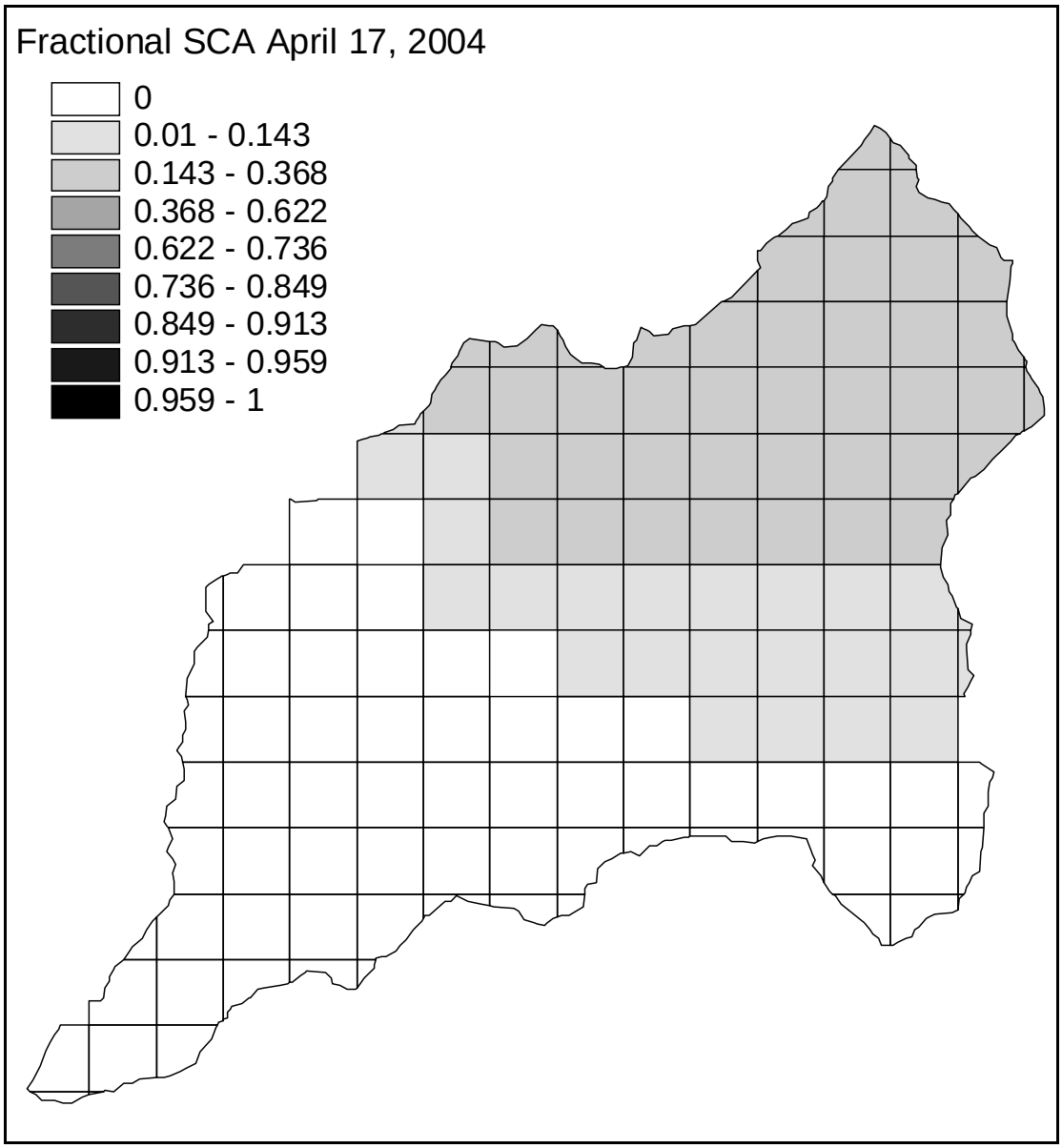

Figure 21. SCA values are displayed by a gray color ramp ranging from from 0 m to 1, 0 being white, and 1 being black. Elements below 1600m in elevation are snow free while all other elevations are between 0.01 and 0.37 snow covered.

4.4 Basin Depletion Curve

The time series data of accumulated melt and fractional snow cover are plotted against one another to produce the Dry Creek depletion curve shown in Figure 22. This curve is produced for the snowmelt event occurring between March 6th 2004 and May 2,

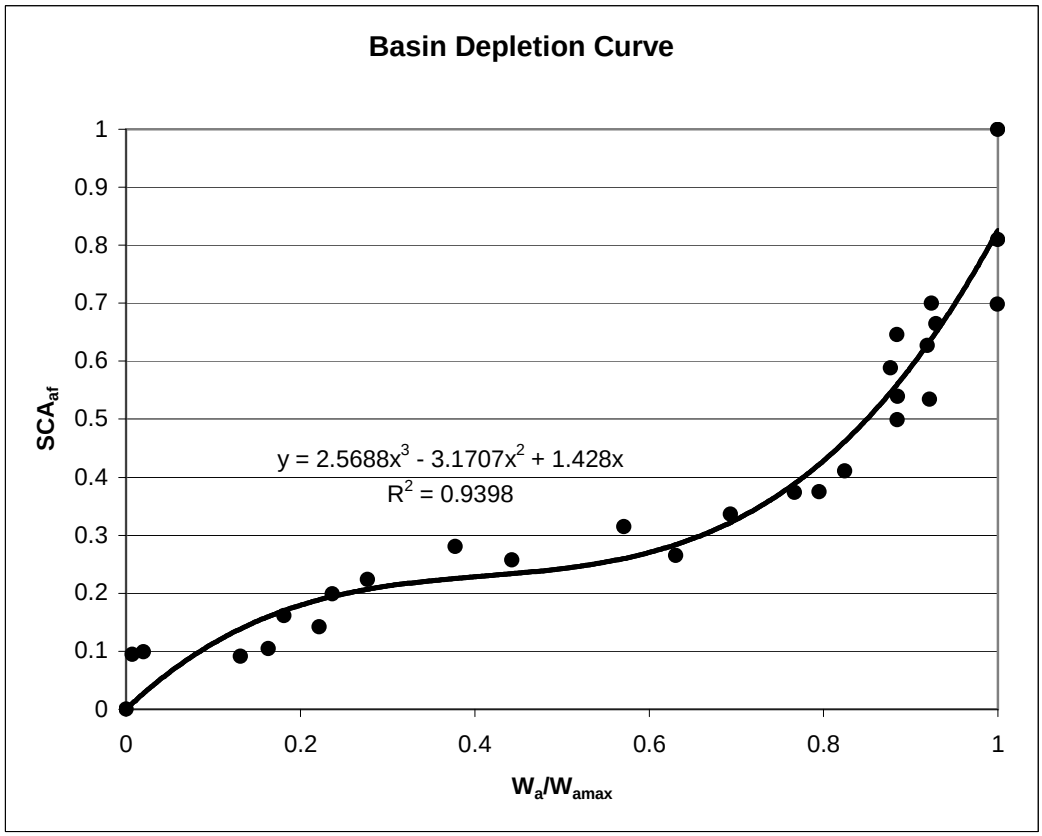

Figure 22. Basin depletion curve. A cubic equation was fit to the data with an R^2 value of 0.939

2004. A cubic equation was fit to the data of the form:

$$SCA_{af} = 2.57\left(\frac{W_a}{W_{a\max}}\right)^3 - 3.17\left(\frac{W_a}{W_{a\max}}\right)^2 + 1.43\left(\frac{W_a}{W_{a\max}}\right) \quad (9)$$

All of the MODIS elements were determined to have zero SCA by May 2, 2004 however; around May 9th to May 12th the basin did receive some additional precipitation in the form of snow. During this event the higher elevation elements were 100% snow covered but the modeled SWE contribution was minimal and therefore skews the results to the SCA axis of the depletion curve. Furthermore, the energy content in the ground after the complete disappearance of snow at lower elevations was such that any new snow quickly melted soon after contact with the ground (minutes to less than 48 hours). Since I am interested in how the reduction of SCA affects the reduction of SWE and elements that received additional snow had already been snow free for many days these points are therefore treated as outliers or excursions when deriving an equation that best fits the data.

4.5 Estimates of Coefficient of Variation

Coefficients of variation are best fit and therefore most reliable for the intermediate depletion curve. This suggests that snow variability can be parameterized with the CV within this elevation band. CV's fit to the higher elevation and lower elevation depletion curves appear to not accurately depict the spatial pattern of snow reduction and therefore cannot be parameterized with just the CV alone. This is most apparent at the onset of melt where data points from the estimated CV deviate greatest from depletion curve data points. The CV fit to the basin depletion curve does not accurately depict the spatial pattern of snow reduction but may provide usefulness in hydrologic modeling at the catchment-scale.

The coefficient of variation for the higher elevation depletion curve is estimated at 1.0. Figure 23 shows the visually fit CV (X's) to the depletion curve plot (circles). The CV for the higher elevation depletion curve is the lowest of all the estimated CV's for the 3 elevation zones. The lower CV suggests that the variability in the snowpack is also low. At the onset of melt there is similarity in the accumulated melt depth spatially with very little change in the area that is covered by snow.

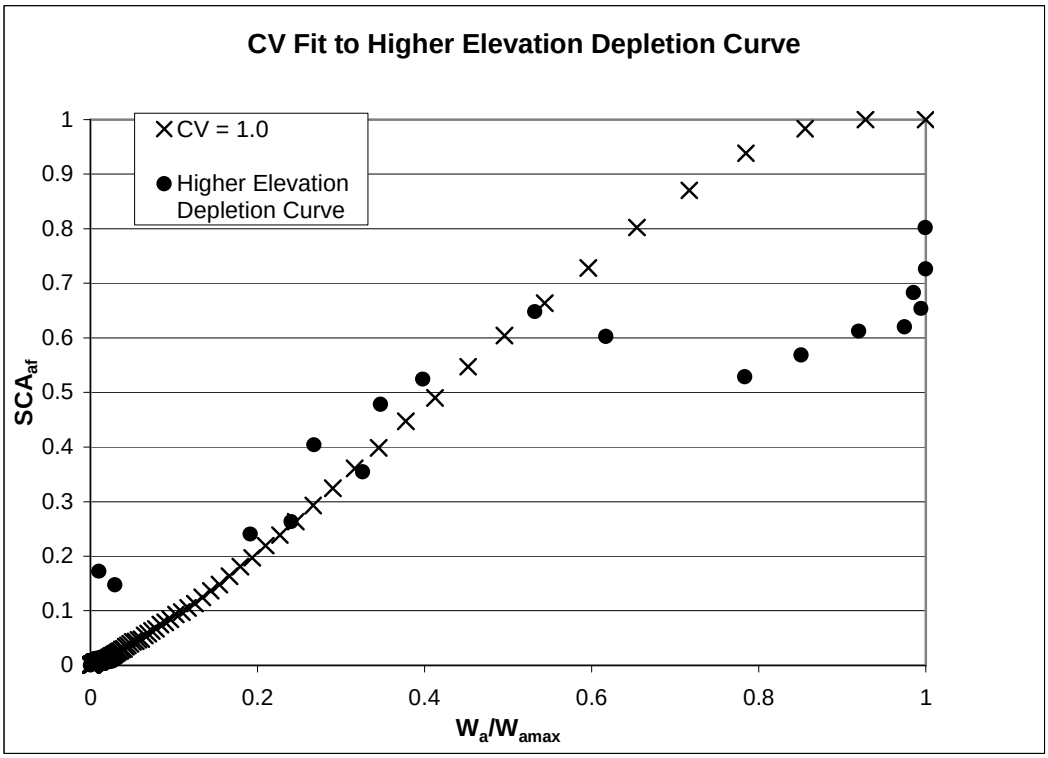

Figure 23. Plot of higher elevation depletion curve and visually fit coefficient of variation of 1.0. The lower CV indicates snow variability is low.

The coefficient of variation for the intermediate elevation depletion curve is estimated at 1.2. Figure 24 shows the visually fit CV (X's) to the depletion curve plot (circles). The higher CV indicates that the variability in snow cover is also higher.

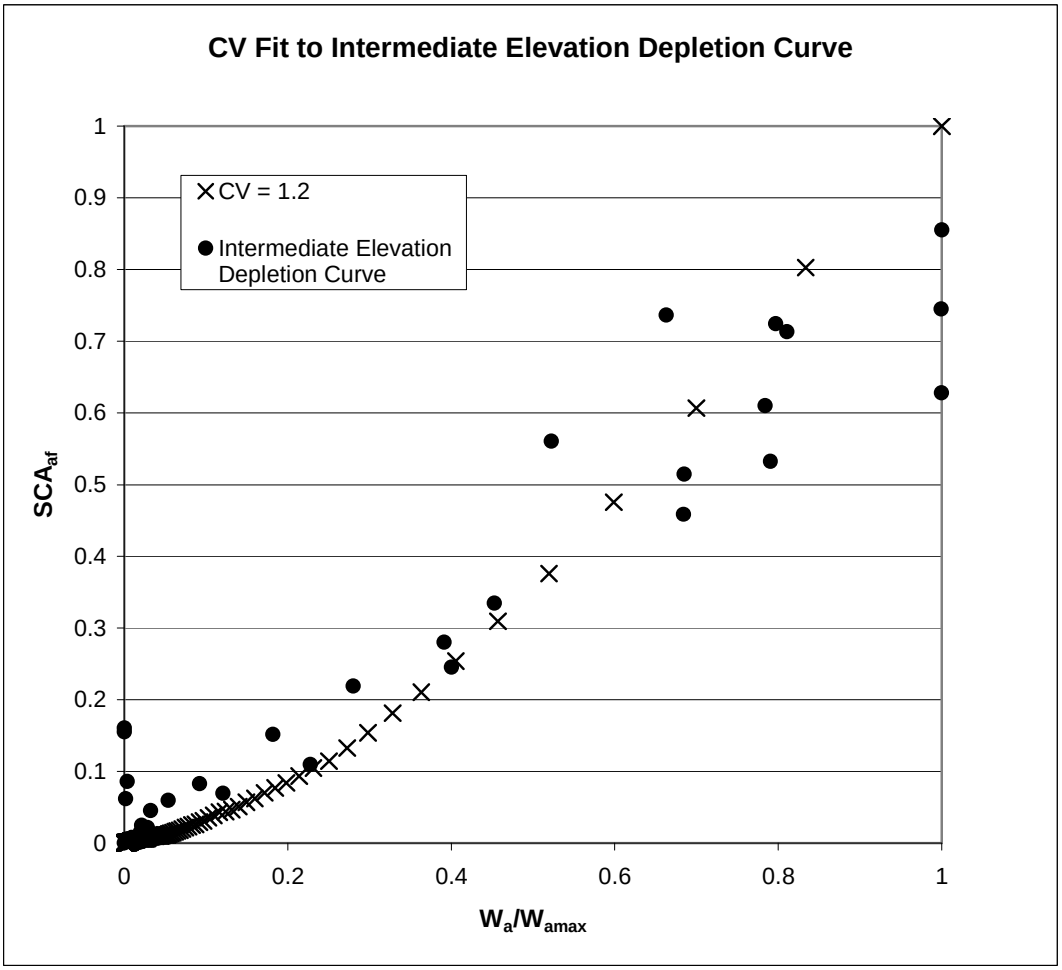

Figure 24. Plot of intermediate elevation depletion curve and visually fit coefficient of variation of 1.2. The lower CV indicates snow variability is low.

The coefficient of variation for the lower elevation depletion curve is estimated at 1.8. Figure 25 shows the visually fit CV (X's) to the depletion curve plot (circles). The fit is poor at the onset of melt but converges toward the end of melt. At these elevations the majority of the landtype exists as either barrenland or sagebrush, the aspect is mostly northwest facing or southeast facing, and lies within a narrow, steep portion of the drainage. This area receives very little precipitation in the form of snow and at the onset

of melt the area is only partially snow covered. Thus the estimated CV is high when compared to the intermediate and higher elevation depletion curves. The implication here is that snow has a bimodal distribution where there are thin layers of snow covering a large area and the remaining area is either uncovered or covered with deeper drifts. The lack of data however, prohibits the use of the estimated CV, as there could easily more variability that is not captured by the curve.

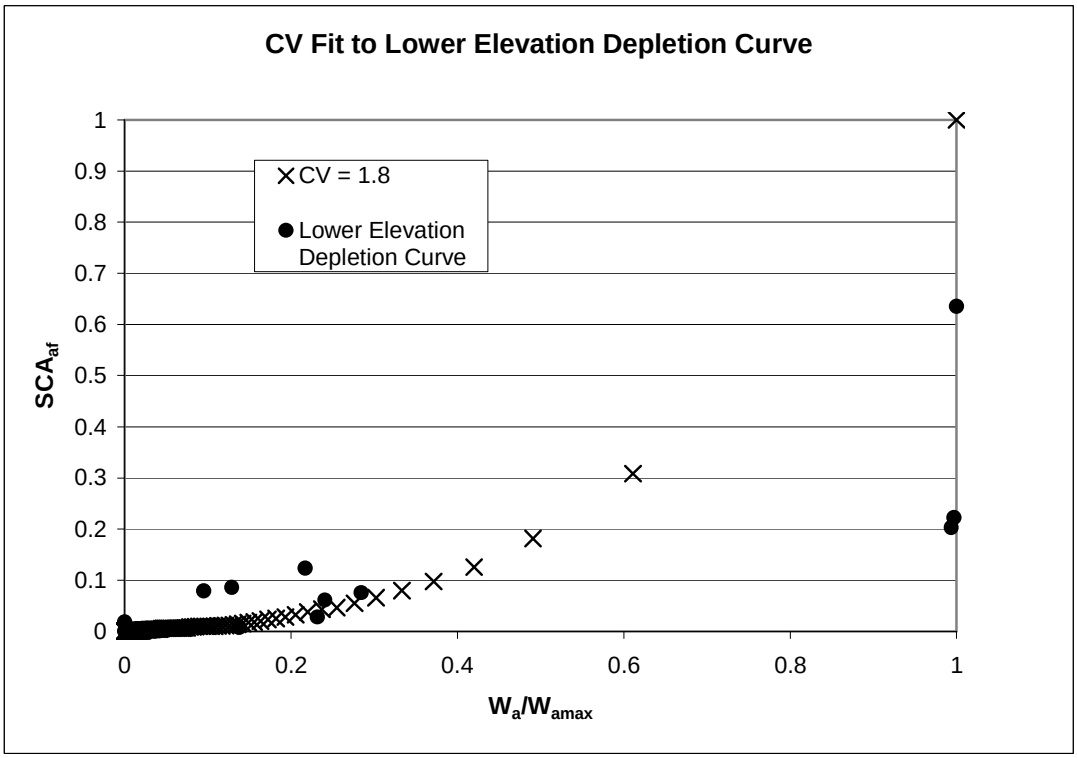

Figure 25. Plot of the lower elevation depletion curve and visually fit coefficient of variation of 1.8. The higher CV indicates higher snow variability.

The coefficient of variation for the basin depletion curve is estimated at 1.5. Figure 26 shows the visually fit CV (X's) to the depletion curve plot (circles).

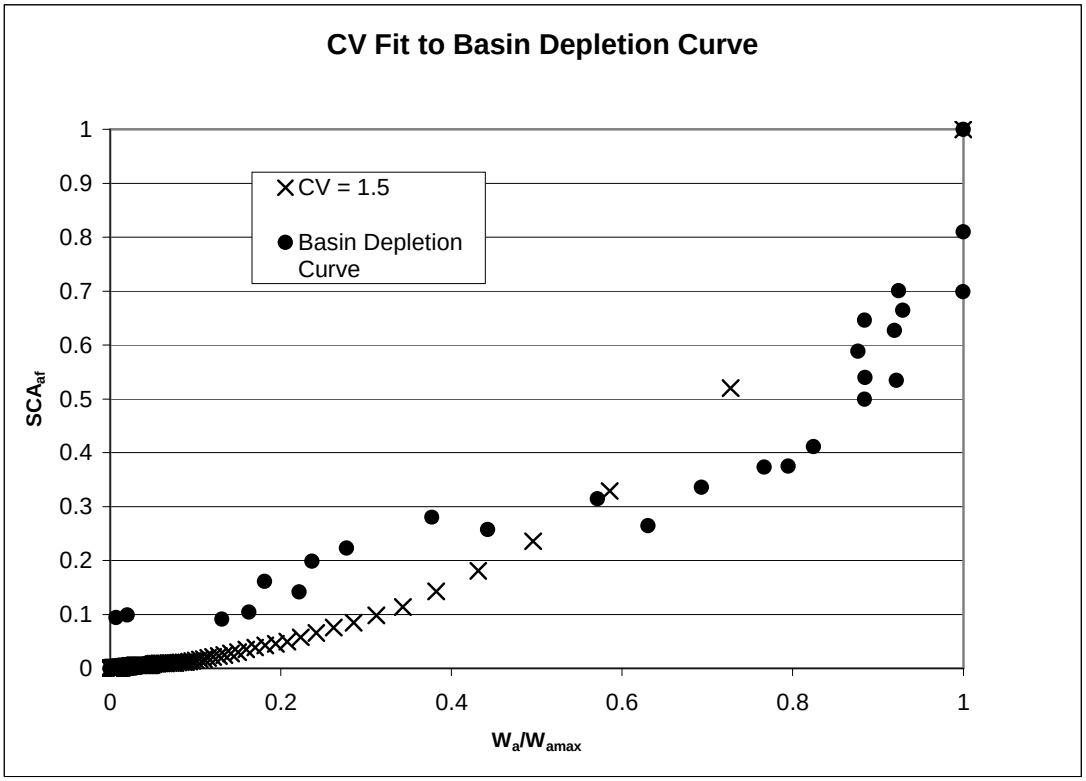

Figure 26. Plot of the basin depletion curve and the visually fit coefficient of variation of 1.5.

4.6 Coefficients of Variations and Snow Survey

The calculated coefficients of variation for elements 3, 10, and 17 are 0.35, 0.33, and 0.39 respectively. A visually fit CV to the depletion curve of each element is 0.35. Figure 27 shows the depletion curve of each element, and the cumulative distribution function of the lognormal distribution with a CV of 0.35. Visually, the calculated CV from spatially sampled SWE values within each element is a good fit to the CV estimated from the depletion curve with the exception of the higher SCA_{af} and higher W_a/W_{amax} values. At the onset of melt the curve indicates that there is a stready increase in the fractional snow cover while the water equivalent values are decreasing. This is

physically impossible and suggests that either error exists in the snowmelt model or in the satellite imagery. Since the model is verified to the Bogus Basin Snotel site with reasonable accuracy, it is likely that the unrealistic shape in the depletion curve can be attributed to the methods used in calculating SCA_{af}. A preliminary investigation was performed on the viewing angles of MODIS satellite scenes. It was determined that increased viewing angles corresponded to decreased calculated SCA_{af}. The satellite, at the nadir view angle (0°) will see more of the snowpack and yield higher SCA_{af} than when the satellite is off-nadir (1°-55°). This bow-tie effect is addressed in Kurt P.

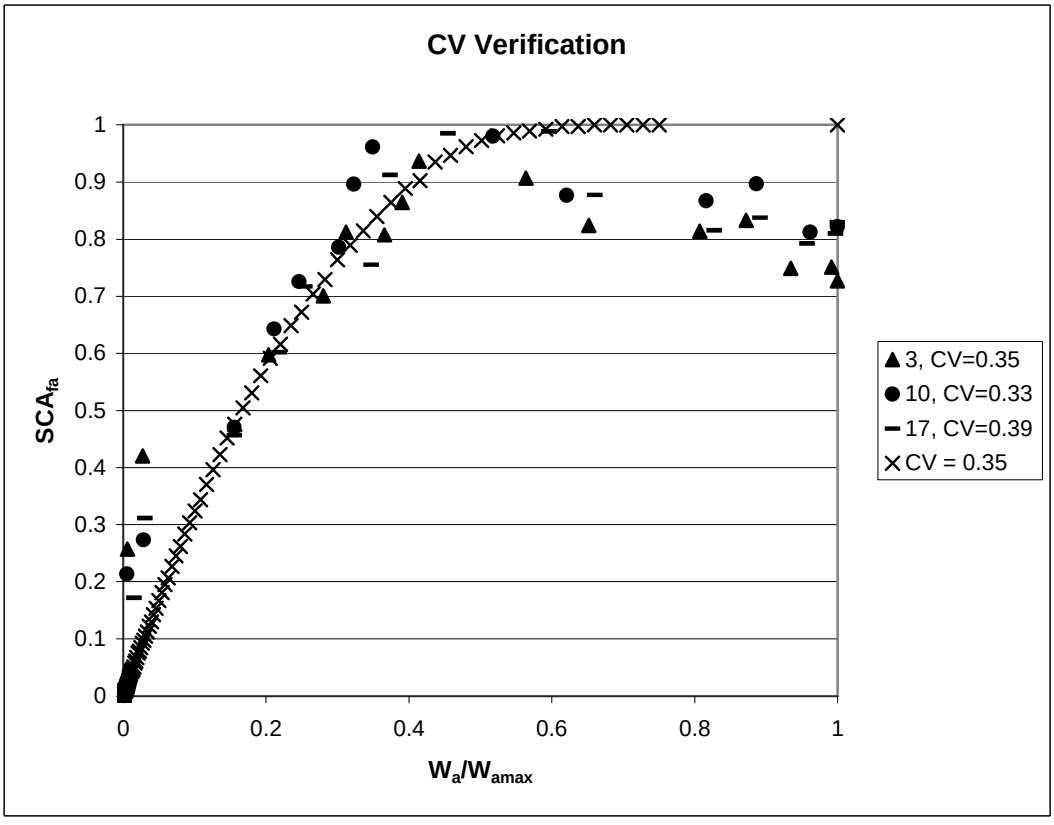

Figure 27. Plot of depletion curves for elements 3, 10, and 17. Calculated coefficients of variation from snow survey data within each element are 0.35, 0.33, and 0.39 respectively. Estimated CV from the shapes of the depletions curves is 0.35. The rise in SCA_{af} at the onset of melt is attributed to the bow-tie effect and possible forest occlusion.

Günther, Stefan W. Maier, Gerhard Gesell, (2002). The increase in SCA_{af} with decreasing W_a/W_{amax} is therefore attributed to this effect. This effect is most apparent on steep slopes with a high forest cover and coincidently terrain of this type exists at the higher elevation elements in the DCEW.

The calculated coefficients of variation for elements 15 and 16 are 0.53 and 0.58 respectively. An estimated CV based on the depletion curves of each element is 0.6 (Figure 28). These results do not absolutely verify this method for parameterizing snow variability, but do provide some insight into other factors affecting the shape of the depletion curve.

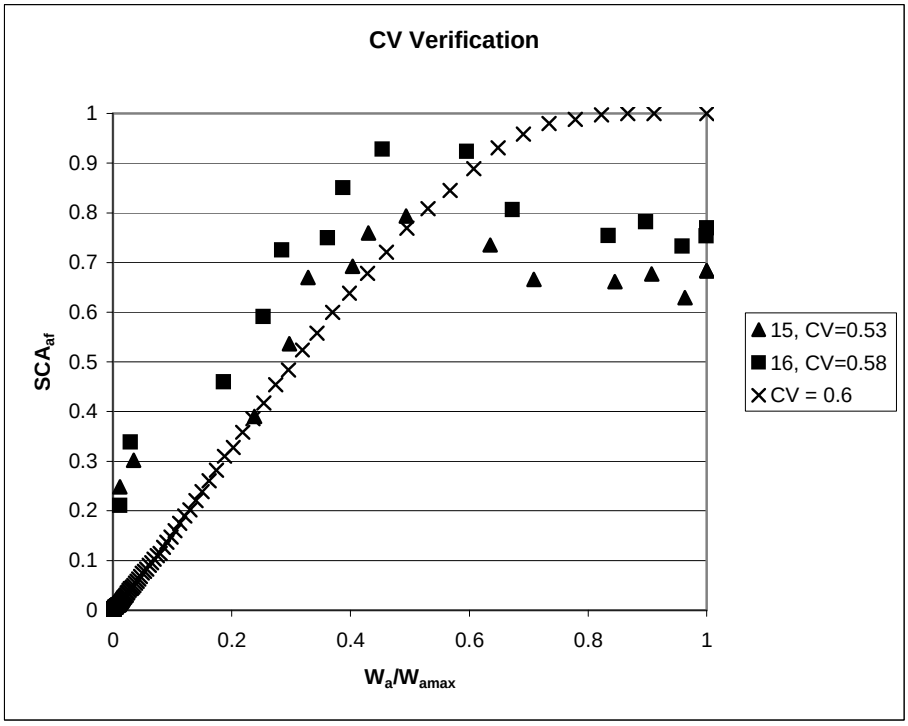

Figure 28. Plot of depletion curves for elements 15 and 16. Calculated coefficients of variation from snow survey data within each element are 0.53 and 0.58 respectively. Estimated CV from the shapes of the depletions curves is 0.6. This does not absolutely verify the method of parameterizing snow variability on the CV as estimated from the depletion curv

4.7 Hydrograph Comparison

There are 4 distinct melt events that occurred in the basin between February 13, 2004 and May 2, 2004. These events are noted by the rapid increase in accumulated melt or change in modeled snow water equivalence. 3 of the 4 events correlate well with spikes observed on the hydrograph. Event 1 corresponds to the rapid increase in melt between February 13th and February 19th, event 2 corresponds to February 22nd to February 19th, event 3 has two parts, the entire event from March 6th to March 23rd, and a sub event between March 17th and March 20th, and event 4 corresponds to March 31st to April 14th. As seen from the hydrograph (Figure 29) between the 28th and 30th of February there is an increase in flow from 2 ft^3/second to about 6.5 ft^3/second. Although the basin has partial snow coverage at higher elevations at this time the flow has no correlation to snowmelt and corresponds to a rain event occurring mainly at lower elevations. It is after this event that the snowpack begins to accumulate to substantial SWE values. Hydrograph response variables are listed in Table 2. Event 1 is the first major melt

Table 2. Table of the hydrograph response variables.

	Event 1	Event 2	Event 3	Sub Event 3	Event 4
Response Lag (days)	3	3	1	4	4
Lag to Peak (days)	5	4	17	6	7

event in the basin and occurs only at the lower elevations. Higher elevations continued to accumulate snow through this time interval. The response lag is 3 days and the lag to peak is 5 days. Event 2 did not contribute significantly to streamflow. There is a small increase in flow of about 1cfs with a response lag of 3 days and a lag to peak of 4 days.

During this time the lower elevation elements that are close in proximity to the gauging station are free of snow. During melt event 2, intermediate elevation elements that are farther upslope of the drainage outlet are the origin of this melt. Because the hillslopes have not yet received sufficient recharge they are hydraulically disconnected from the stream. Once the hillslope is connected there is an immediate stream response to snowmelt beginning with event 3. Event 3 is the most major melt event occurring in the basin and in turn contributes the most to streamflow. The melt occurring during the peak of event 3 (dotted oval in Figure 29) is considered a sub-event with a response lag of 4 days and a lag to peak of 6 days. Event 4 is a late melt event with a response lag of 4 days and lag to peak of 6 days. Event 4 is unique in that melt continues to occur while the hydrograph drops along the recessional limb. This is probably due to the way the remaining snow is distributed in the basin. All of the snowmelt is constrained to locally limited drifts and the uncovered hillslopes continue to drain without further input. Thus, the flow through the hillslope to the stream, while governed by darcys law is limited by the capacity to transmit fluid through its porous medium from a minimal number of point locations in the basin.

The general trend of the hydrograph response variables is that the lags are increasing through the melt period during each successive melt event. This suggests that the source or entry point of melt water from the snowpack is farther away from the drainage outlet. This is consistent with field observations of the locations of the remaining snowpack throughout the basin.

The total volume of water as event flow (with baseflow subtracted) is 2,809,362 m^3 and the total volume of water as input (snowmelt) is 2,541,875 m^3. The difference of about 300,000 m^3 can be attributed to rain and rain on snow events that are not simulated. The results however, demonstrate that the measured runoff is of the same order of magnitude as the modeled snowmelt available for runoff and thus provide a qualitative evaluation of the model.

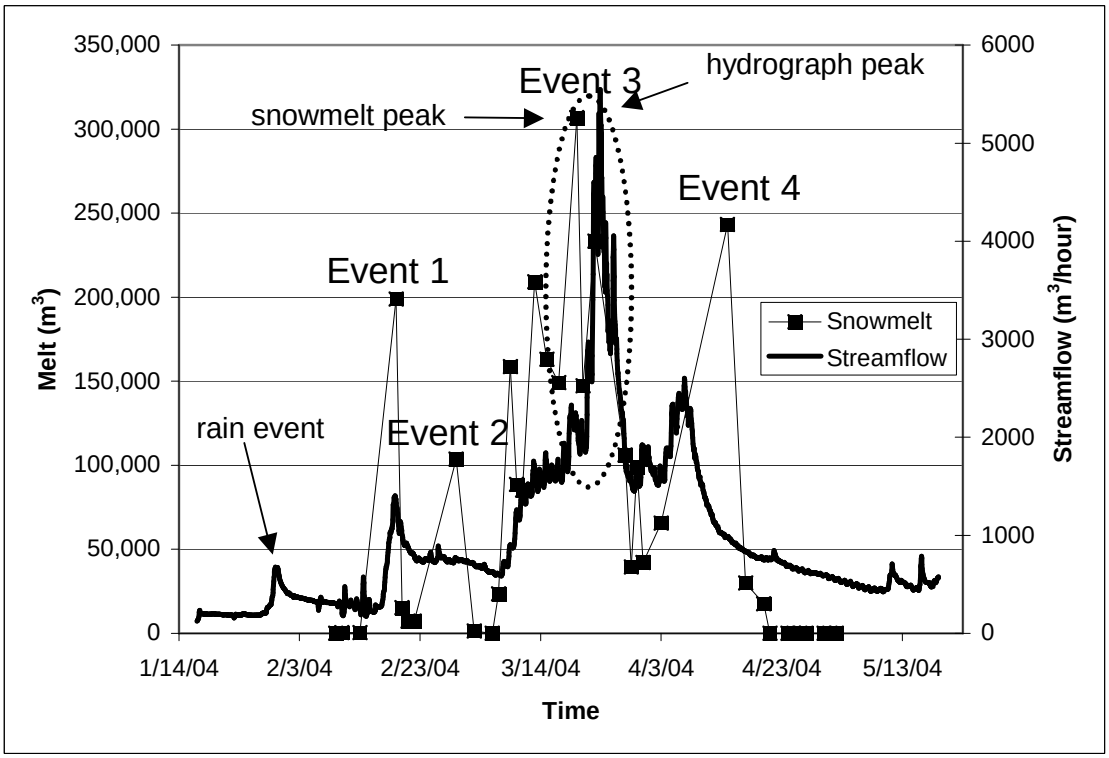

Figure 29. Time series of the Dry Creek Hydrograph and modeled melt. 4 melt events are noted and hydrograph response variables are calculated. The response lags and lags to peak are increasing through the melt period during each successive melt event. This suggests that the source or entry point of melt water from the snowpack is farther away from the drainage outlet. The total volume of event flow is 2,809,362 m^3 and the total volume of water as input (snowmelt) is 2,541,875 m^3. These results verify the model and provide some quantitative assessment of snowmelt and subsequent streamflow.

5 EXAMPLE APPLICATION

The results of this research are intended to be used in hydrologic models to aid in the prediction of snowmelt generated streamflow. An example of such an application is given below.

Snowmelt-Runoff Model (SRM) uses modified snow cover depletion curves (MDC's) that relate fractional snow cover to snowmelt depth. The basis of this approach is that patterns of disappearing snow cover are similar year after year and that associated snowmelt depths can be predicted based on that pattern. The results presented here suggest that once the depletion curves have been established the functional form can be used during successive years to predict melt outflow from the snowpack. The melt outflow can then be routed through the hillslope and channel network within SRM. This type of depletion curve may substitute entirely for the MDC's used in SRM or may serve as a calibration in which to drive the model. The delivery of snowmelt to the stream from lower elevations is therefore related to the depletion curve established for those particular elevations and not the depletion curve established for the entire basin.

6 CONCLUSIONS

Repeat measurements of remotely sensed SCA combined with a distributed mass and energy balance model improve methods for establishing a graphical representation of the depletion of snow in the DCEW. Therefore the depletion of snow in the DCEW can be characterized with the derived depletion curve. Snow variability decreases with increasing elevation as suggested by estimated CV's. However, estimated CV's are not necessarily a good representation of the subgrid variability of snow at the scale of 500 m^2 and suggest that there is scale dependence. The difference in the estimated CV's at the modeled scale (500 m^2) versus the measured scale (sub 500 m^2) suggests that the variability in snow cover is not captured. However, the off-nadir effects on calculated SCA_{af} skew the estimated CV at the measurement scale (CV = 0.3 - 0.6) to lower values than those CV's estimated at the model scale (CV = 1). Therefore, it is possible that there is much smaller scale dependence than is suggested.

7 REFERENCES

Anderson, E. A., 1973. National Weather Service River Forecast System-Snow Accumulation and Ablation Model. NOAA Technical Memorandum NWS HYDRO-17, U.S. Dept. of Commerce, Silver Spring, Maryland.

Anderson, E. A., 1976. A Point Energy and Mass Balance Model of a Snow Cover. NOAA Technical Report NWS 19, U.S. Dept. of Commerce.

Blöschl, G., 1999. Scaling issues in snow hydrology. Hydrological Processes 13: 2149–2175.

Bristow, K. L., and G. S. Campbell, 1984. On the Relationship Between Incoming Solar Radiation and the Daily Maximum and Minimum Temperature. Agricultural and Forest Meteorology, 31: 159-166.

Brutsaert, W., 1982. Evaporation into the Atmosphere. Kluwer Academic Publishers, 299 p.

Cline, D. W., R. C. Bales and J. Dozier, 1998. Estimating the Spatial Distribution of Snow in Mountain Basins Using Remote Sensing and Energy Balance Modeling. Water Resources Research, 34(5): 1275-1285.

Déry, S. J., Salomonson, V. V., Stieglitz, M., Hall, D. K., and Appel, I., 2005. An approach to using snow areal depletion curves inferred from MODIS and its application to land surface modelling in Alaska, Hydrol. Proc, 19, 2755-2774

Dewalle, D.R., Z. Henderson, and A. Rango, 2002. Spatial And Temporal Variations In Snowmelt Degree-Day Factors Computed From Snotel Data In The Upper Rio Grande Basin. Proceedings Of The Western Snow Conference. p. 73-81.

Dickinson, R. E., A. Henderson-Sellers and P. J. Kennedy, 1993. Biosphere-Atmosphere Transfer Scheme (BATS) Version 1e as Coupled to the NCAR Community Climate Model. NCAR/TN-387+STR, National Center for Atmospheric Research.

Dingman, S. L., 1994. Physical Hydrology. Macmillan, 575 p.

Koskinen, J., J. Pulliainen, and M. Hallikainen, 1997. The Use of ERS-1 SAR Data in Snow Melt Monitoring, IEEE Trans. on Geoscience and Remote Sensing, 35(3): pp. 601-610.

Liston, G. E., 2005. Global Snow-Water Equivalent Depth Coefficient-of-Variation Classification. Boulder, CO: National Snow and Ice Data Center. Digital media.

Lowe, P. R., 1977. An Approximating Polynomial for the Computation of Saturation Vapour Pressure. Journal of Applied Meteorology, 16: 100-103.

Luce C.H., D.G., Tarboton, and K. R. Cooley, 1999. Subgrid parameterization of snow distribution for an energy and mass balance snow cover model. Hydrological Processes 13: 1921–1933.

Luce, C.H., and D.G., Tarboton, 2004. The Application of Depletion Curves for Parameterization of Subgrid Variability of Snow. Hydrological Processes, 18: 1409-1422, DOI: 10.1002/hyp.1420.

Male, D. H. and D. M. Gray, 1981. Snowcover Ablation and Runoff. Chapter 9 in Handbook of Snow, Principles, Processes, Management and Use, Edited by D. M. Gray and D. H. Male, Pergammon Press, p.360-436.

Martinec, J., A. Rango, and R. Roberts, 1998. Snowmelt Runoff Model (SRM) User's Manual. Geographica Bernensia. Department of Geography, University of Bern, 84 pp.

MODIS homepage: http://modis.gsfc.nasa.gov/.

MODIS data: http://edcimswww.cr.usgs.gov/pub/imswelcome/.

Mote, T. L., A. J. Grundstein, D. J. Leathers, and D. A. Robinson, 2003. A comparison of modeled, remotely sensed, and measured snow water equivalent in the northern Great Plains. Water Resources Research, 39(8), 1209.

Price, A. G. and T. Dunne, 1976. Energy balance computations of snowmelt in a subarctic area. Water Resources Research, 12(4): 686-694.

Redmond, R. L., T. P. Tady, F. B. Fisher, M. Thornton, and J. C. Winne., 1997. Landsat vegetation mapping of the southwest and central Idaho ecogroups. Montana Cooperative Wildlife Research Unit, The University of Montana, Missoula. 42 pp.

Riley, J. P., D. G. Chadwick and J. M. Bagley, 1966. Application of electronic analog computer to solution of hydrologic and river basin planning problems: Utah simulation model II," PRWG32-1. Utah Water research lab., Utah State University.

Rosenberg, N. J., 1974. Microclimate The Biological Environment, John Wiley & Sons, Inc., 315 p.

Salomonson, V.V. and I. Appel, 2004. Estimating the fractional snow covering using the normalized difference snow index. Remote Sensing of Environment, 89(3):351-360.

Satterlund, D. R., 1979. An Improved Equation for Estimating Long-wave Radiation From the Atmosphere. Water Resources Research, 15: 1643-1650.

Susong, D., D. Marks, and D. Garen, 1999. Methods for developing time-series climate surfaces to drive topographically distributed energy- and water-balance models. Hydrological Processes, vol. 13, no. 13-14, pp. 2003-2021.

Swamy A. N. and P.A. Brivio, 1997. Modelling runoff using optical satellite remote sensing data in high mountainous alpine catchment of Italy. Hydrological Processes, John Wiley & Sons, Chichester, vol. 11, pp. 1475-1491.

Tarboton D.G., and C.H., Luce, 1996. Utah energy balance snow accumulation and melt model (UEB), computer model technical description and users guide. Utah Water Research Laboratory and USDA forest service intermountain research station. (http://www.engineering.usu.edu/dtarb/) Accessed 10 January 2004.

U.S. Army Corps of Engineers, 1956. Snow Hydrology, Summary report of the Snow Investigations. U.S. Army Corps of Engineers, North Pacific Division, Portland, Oregon.

USDA, 1974. Soil Hydrologic Reconnaissance Survey. Forest Service, Boise Idaho.

Yenko, M., 2003. Hydrometric and Geochemical Evidence of Streamflow Sources in the Upper Dry Creek Experimental Watershed, Southwestern Idaho. Masters thesis, Boise State University, Boise Idaho.

8 APPENDIX A

UEB Model Description

The UEB model was developed by David G. Tarboton and Charles H. Luce through a cooperative agreement between Utah Water Research Laboratory, Utah State University, and USDA Forest Service, Intermountain Research Station, 1996. These two state variables are updated according to

$$dU/dt = Q_{sn}+Q_{li}-Q_{le}+Q_p+Q_g+Q_h+Q_e-Q_m \quad (10)$$

$$dW/dt = P_r+P_s-M_r-E \quad (11)$$

where Q_{sn} is net solar radiation; Q_{li} is incoming longwave radiation; Q_{le} is outgoing longwave radiation; Q_p is advected heat from precipitation; Q_g is ground heat flux; Q_h is the sensible heat flux; Q_e is the latent heat flux; Q_m is heat advected with melt water; P_r is the rate of precipitation as rain; P_s is the rate of precipitation as snow; M_r is the melt rate; and E is the sublimation rate. The model is driven by inputs of air temperature, precipitation, wind speed, humidity, and radiation at time steps sufficient to resolve the diurnal cycle (hourly or six hourly), (Tarboton and Luce, 1996). Melt outflow is a function of liquid fraction which is essentially the average snowpack temperature calculated from the energy content. The model uses physically based calculations of radiative, sensible, latent, and advective heat exchanges. See Tarboton and Luce, 1996 for a technical description and user guide.

Shortwave Radiation and Albedo

Net shortwave radiation is calculated as:

$$Q_{sn} = Q_{si}(1-A) \quad (12)$$

where A is albedo and Q_{si} incident shortwave radiation measured by a horizontally mounted pyranometer. If measured shortwave radiation is not available it can be

estimated from the diurnal temperature range following Bristow and Campbell, 1984. Incident shortwave (solar) radiation is calculated by:

$$Q_{si} = Q_m * \frac{HRI}{HRI_0} \tag{13}$$

where HRI is a multiplication factor adjusted by the integral of the solar illumination angle as follows:

$$HRI = \frac{1}{\cos(\theta) * \Delta t} \int_t^{t+\Delta t} \cos(\psi) dt \tag{14}$$

and HRI_0 is the multiplication factor (HRI) evaluated at zero slope. θ is the local slope derived from a DEM and ψ is the illumination angle. This integral is evaluated using the concept of equivalent slope (e.g. Riley, Chadwick and Bagley, 1966; or Dingman, 1994) to account for the dependence of the position of the sun on season, latitude and time of day and adjust for slope and aspect. Incident shortwave radiation calculated in this way effectively adjusts horizontally measured radiation to a sloping surface.

Albedo is calculated as a function of snow surface age and solar illumination angle following Dickinson et al., 1993, p21. Snow age is adjusted with each time step according to snow surface temperature and new snowfall. Albedo is computed by taking the average of the visible (< 0.7 μm) and near infrared (> 0.7 μm) reflectances. Slope and illumination angle are used to adjust calculations from a horizontal reference. Diffuse reflectances are computed by:

$$\alpha_{vd} = (1 - C_v * F_{age})\alpha_{vo} \tag{15}$$

$$\alpha_{ird} = (1 - C_{ir} * F_{age})\alpha_{iro} \tag{16}$$

where α_{vd} and α_{ird} are diffuse reflectances in the visible and near infrared bands respectively. F_{age} is a function that adjusts snow surface age by simulating grain size growth as a function of time and vapor diffusion. $C_v = 0.2$ and $C_{ir} = 0.5$ are parameters that quantify grain size growth, and $\alpha_{vo} = 0.85$ and $\alpha_{iro} = 0.65$ are fresh snow reflectances in each band. F_{age} is given by:

$$F_{age} = \frac{\tau}{1 + \tau} \tag{17}$$

where τ is a snow surface age coefficient that is evaluated for each time step by:

$$\Delta\tau = \frac{r_1 + r_2 + r_3}{\tau_o} * \Delta t \tag{18}$$

Δt is the time step in seconds with $\tau_o = 106$ s. r_1 is a parameter that changes as a function of snow surface temperature, T_s [°K], and represents grain growth due to vapor diffusion.

$$r_1 = \exp\left[5000\left(\frac{1}{273.16}\right) - \frac{1}{T_s}\right] \tag{19}$$

r_2 is a parameter that accounts for freezing and near freezing conditions common during melt and refreeze events:

$$r_2 = \min\left(r_1^{10}, 1\right) \tag{20}$$

r_3 is a parameter that accounts for the effect of dirt and soot = 0.03 (0.01 in Antarctica). The snow surface is restored when 0.01 m of snowfall is accumulated over the time step ($\tau = 0$). When snowfall, $P_s < 0.01$ m snow surface age is reduced by $(1 - 100P_s)$. The

reflectance of radiation with illumination angle ψ (measured relative to the surface normal) is computed as

$$\alpha_v = \alpha_{vd} + 0.4 f(\psi)(1-\alpha_{vd}) \tag{21}$$

$$\alpha_{ir} = \alpha_{ir} + 0.4 f(\psi)(1-\alpha_{ird}) \tag{22}$$

where

$$f(\psi) = \frac{1}{b}\left[\frac{b+1}{1+2b*\cos(\psi)} - 1\right] for \cos(\psi) < 0.5 \tag{23}$$

= 0 otherwise

where b = 2 set by Dickinson et al., 1993, p21., cos(60) = 0.5, and illumination angles greater than 60° are computed to increase the reflectances. When the snowpack is less than 0.1 m albedo is interpolated between the snow albedo A_s and bare ground albedo A_{bg} by:

$$A = r * A_{bg} + (1-r)A_s \tag{24}$$

and

$$r = \left(1 - \frac{z}{h}\right)\exp^{\frac{-z}{2h}} \tag{25}$$

Longwave Radiation

Outgoing longwave radiation is

$$Q_{le} = \varepsilon_s * \sigma * T_s \tag{26}$$

where ε_s is emissivity, σ the Stefan Boltzmann constant [2.07 x 10-7 kJ m-2 hr-1 °K-4] and T_s is absolute temperature [K]. Incoming longwave radiation is estimated using the Stefan-Boltzmann equation:

$$Q_{li} = \varepsilon_a * \sigma * T_a \tag{27}$$

where (ε_a)is air emissivity and (T_a in kelvin) is air temperature. Emissivity for clear sky conditions is calculated following Satterlund, 1979:

$$\varepsilon_{acls} = 1.08\left[1 - \exp\left(-\left(\frac{e_a}{100}\right)^{\frac{T_a}{20167}}\right)\right] \tag{28}$$

To adjust for cloud cover fraction (CF) the following is computed following Bristow and Campbell, 1984:

$$CF - 1 - \frac{T_f}{a} \tag{29}$$

where the transmission factor (T_f) is computed by :

$$T_f = \frac{Q_m}{I_o * HRI_o} \tag{30}$$

where HRI_o is found from equation 5. Then air emissivity is calculated by:

$$\varepsilon_a = CF + (1 - CF)\varepsilon_{acls} \tag{31}$$

Snow fall accumulation and heat with precipitation

Measured precipitation rate P, is partitioned into rain P_r, and snow P_s, (both in terms of water equivalence depth) using the following rule based on air temperature T_a, (U.S. Army Corps of Engineers, 1956)

$$\Pr = P \qquad T_a \geq T_r = 3°C \tag{32}$$

$$\Pr = P\frac{T_a - T_b}{T_r - T_b} \qquad T_b < T_a < T_r \tag{33}$$

$$P_r = 0 \qquad T_a \leq T_b + -1°C \tag{34}$$

$$P_s = (P - P_r)F \tag{35}$$

where precipitation accumulates as rain if the temperature of air is greater or equal to 3ºC. Precipitation accumulates as snow if the air temperature is less than or equal to -1ºC.

The redistribution of snow is accounted for in the model through a snow drift factor, F, where values greater than 1 correspond to deposition sinks and values less than 1 correspond to locations of wind scour. In this study the drift factor was calibrated based on the date at which snow covered area goes to zero. The developers of the model adjusted this factor on a basis of visual observation. This approach treats drifting as occurring at snowfall rather after snowfall, and therefore assumes that the snowmelt model correctly accounts for all other processes (melt, sublimation, condensation, etc.)

affecting the accumulation and ablation of snow water equivalence (Tarboton and Luce 1996).

The energy required to convert precipitation to 0°C is the advected heat, computed by:

$$Q_p = P_s * C_s * \rho_w * \min(T_a,0) + P_r \left[h_f * \rho_w + C_w \rho_w * \max(T_a,0) \right] \quad (36)$$

Turbulent fluxes, Q_h, Q_e, E

Sensible and latent heat fluxes between the snow surface and air above are modeled using the concept of flux proportional to temperature and vapor pressure gradients (Tarboton and Luce, 1996). Turbulent transfer coefficients vary as a function of windspeed and surface roughness. Heat transport towards the surface, Q_h [kJ/m2/hr] is given by:

$$Q_h = K_h * \rho_a * C_p (T_a - T_s) \quad (37)$$

where ρ_a is air density, C_p air specific heat capacity [1.005 kJ kg-1 oC-1], K_h is heat conductance [m/hr] and T_s is the snow surface temperature, T_a is the air temperature. Vapor transport away from the surface (sublimation), M_e [kg/hr] is:

$$M_e = K_e * \rho_a (q_s - q) \quad (38)$$

where q_s is the surface specific humidity and K_e the vapor conductance [m/hr].
From Anderson, 1976; Male and Gray, 1981; Brutsaert, 1982 the following expression is obtained:

$$K_h = K_e = K_{nuetral} = \frac{k^2 * V}{\left[\ln\left(\frac{z}{z_0}\right)^2\right]} \tag{39}$$

where V is wind speed [m/hr] at height z [m]; z_o is roughness height at which the logarithmic boundary layer profile predicts zero velocity [m]; and k is von Karman's constant [0.4] (Tarboton and Luce, 1996). The Richardson number or Monin-Obukhov length is used to account for the effects of temperature gradients near the surface by:

$$R_i = \frac{\left(\frac{g}{T}\right)\frac{dT}{dz}}{\left(\frac{dV}{dz}\right)^2} \approx \frac{g(T_a - T_s)z}{V^2 * T_a} \tag{40}$$

Heat and vapor conductances K_h and K_e and are adjusted following (Price and Dunne, 1976):

$$K_{adj} = \frac{K_{nuetral}}{(1+10 * R_i)} \qquad R_i > 0, \text{ Stable or inversion conditions} \tag{41}$$

$$K_{adj} = \frac{K_{nuetral}}{(1-10 * R_i)} \qquad R_i < 0, \text{ Unstable or lapse conditions} \tag{42}$$

Latent heat flux towards the snow is:

$$Q_e = h_v * M_e \tag{43}$$

and specific humidity, vapor pressure and the ideal gas law are used to obtain:

$$Q_e = K_e\left(\frac{h_v * 0.622}{R_d * T_a}\right)\left(e_a - e_s(T_s)\right) \tag{44}$$

where e_s is the vapor pressure at the snow surface snow, assumed saturated at T_s, and calculated using a polynomial approximation (Lowe, 1977); ea is air vapor pressure, R_d is the dry gas constant [287 J kg-1 K-1] and h_v the latent heat of sublimation [2834 kJ/kg] (Tarboton and Luce, 1996).

The water equivalence depth of sublimation is:

$$E = -\frac{Q_{ev}}{\rho_w * h_v} \tag{45}$$

Snow Surface Temperature, T_s

An equilibrium approach that balances energy fluxes at the snow surface is used to account for differences in temperatures of the snowpack and at the snow/air interface. Heat conduction into the snow is calculated by:

$$Q = \frac{\kappa * \rho_s * C_s (T_s - T)}{Z_e} = K_s * \rho_s * C_s (T_s - T) \tag{46}$$

where κ is snow thermal diffusivity [m^2 hr-1] and Z_e [m] an effective depth over which this thermal gradient acts. The ratio κ/Z_e is denoted by K_s and termed snow surface conductance, analogous to the heat and vapor conductance. A value of K_s is obtained by assuming a depth Z_e equal to the depth of penetration of a diurnal temperature fluctuation calculated from:

$$\frac{R_z}{R_s} = \exp\left(-z\left(\frac{\pi}{\alpha P}\right)^{1/2} \right) \tag{47}$$

following Rosenberg, 1974, where R_s is the range of temperature oscillation at the surface, R_z is the range of temperature oscillation at depth z, P is the period of oscillation, and α is the thermal diffusivity. Z_e should be chosen so that R_z/R_s is small. Here K_s is used as a tuning parameter, with this calculation used to define a reasonable range (Tarboton and Luce, 1996). The surface energy balance gives:

$$Q = Q_{sn} + Q_{li} + Q_h(T_s) + Q_e(T_s) + Q_p + Q_{le}(T_s) \tag{48}$$

Meltwater Outflux, M_r and Q_m

The energy content variable U determines the liquid content of the snowpack. As coupled with Darcy's law determines the outflow rate.

$$M_r = K_{sat} * S^{*3} \tag{49}$$

where K_{sat} is the snow saturated hydraulic conductivity and S* is the relative saturation in excess of water retained by capillary forces. This expression is based on Male and Gray (1981, p. 400, eqn 9.45). S* is given by:

S* = (liquid water volume - capillary retention)/(pore volume - capillary retention)=

$$\frac{\left(\frac{L_f}{1-L_f} - L_c\right)}{\left(\frac{\rho_w}{\rho_s} - \frac{\rho_w}{\rho_i} - L_c\right)} \tag{50}$$

where $L_f = U/(\rho_w h_f W)$ is the proportion of the snowpack that is liquid, L_c [0.05] the capillary retention as a fraction of the solid matrix water equivalence, and ρ_i the density of ice [917 kg m-3] (Tarboton and Luce, 1996). The melt outflow is then:

$$Q_m = \rho_w * h_f * M_r \tag{51}$$

8.1 Model Parameters

The following are a list of model parameters used to compute the energy budget calculations in UEB;

1. T_r Temperature above which all precipitation is rain (3 °C).

2. T_s Temperature below which all precipitation is snow (-1 °C).

3. T_o Temperature of freezing (0 °C).

4. TK Constant to convert °C to Kelvin (273.15).

5. ε_s emissivity of snow (nominally 0.99).

6. σ Stefan boltzman constant (2.0747e-7 kJ/m2/hr/K).

7. h_f Heat of fusion (333.5 kJ/kg).

8. h_v Heat of Vaporization (Ice to Vapor, 2834 kJ/kg).

9. C_w Water Heat Capacity (4.18 kJ/kg/C).

10. C_s Ice heat capacity (2.09 kJ/kg/C).

11. C_g Ground heat capacity (nominally 2.09 kJ/kg/C).

12. C_p Air Heat Capacity (1.005 kJ/kg/K).

13. R_d Ideal Gas constant for dry air (287 J/kg/K).

14. k Von Karman's constant (0.4).

15. z Nominal measurement height for air temperature and humidity (2 m).

16. z_o Surface aerodynamic roughness (m).

17. HFF Factor to convert hours into seconds (3600).

18. ρ_i Density of Ice (917 kg/m3).

19. ρ_w Density of Water (1000 kg/m3).

20. ρ_s Snow Density (nominally 450 kg/m3).

21. ρ_g Soil Density (nominally 1700 kg/m3).

22. L_c Liquid holding capacity of snow (0.05).

23. K_{sat} Snow Saturated hydraulic conductivity (20 m/hr).

24. D_e Thermally active depth of soil (0.4 m).

25. K_s Snow Surface thermal conductance (m/hr).

26. g Gravitational acceleration (9.81 m/s2).

27. A_{bg} Bare ground albedo (0.25).

28. α_{vo} New snow visible band reflectance (0.85).

29. α_{iro} New snow near infrared band reflectance (0.65).

30. F_{stab} Stability correction control parameter (0).